



Turbulence variability in the upper layers of the Southern Adriatic Sea under a variety of atmospheric forcing conditions

Sandro Carniel ^{a,*}, Lakshmi H. Kantha ^{a,b,1,2}, Jeffrey W. Book ^c, Mauro Sclavo ^{a,1}, Hartmut Prandke ^{d,3}

^a CNR-ISMAR, Castello 2737F, 30122 Venice, Italy

^b Department of Aerospace Engineering, University of Colorado, Boulder, CO, USA

^c US Naval Research Laboratory, Stennis Space Center, MS, 39529 USA

^d ISW Wassermesstechnik, Gartenweg 1, Petersdorf, Germany

ARTICLE INFO

Article history:

Received 23 June 2010

Received in revised form

24 December 2010

Accepted 11 January 2011

Available online 19 January 2011

Keywords:

Turbulent mixing

Microstructure

Mixing processes

ABSTRACT

As part of the DART06B observational campaign in late August 2006, a microstructure profiler was deployed to make turbulence measurements in the upper layers of the Southern Adriatic Sea. Of the nearly 300 total casts, 163 were made near Station B90, where various moorings were deployed in the 90 m deep water column to measure water column properties and meteorological and surface wave conditions. We were able to measure turbulence properties in the upper layers under a variety of atmospheric forcing conditions that included strong wind forcing, night-time convection, mixed convection and wind forcing, weak wind forcing and strong insolation. The resulting dataset provides a kaleidoscope of turbulence properties and turbulent mixing above, below and in the strong pycnocline present at a depth of 15–25 m in the coastal waters of the Southern Adriatic Sea during late summer. A slightly modified scaling of the dissipation rate of turbulence kinetic energy in the Mixed Layer (ML), based on the observed friction velocity u_* and the surface buoyancy flux J_{bo} , reproduces the measured values reasonably well. In the interior, below the ML, the dissipation rate scales like $L_7^4 N^3$, where L_7 is the Thorpe scale and N is the buoyancy frequency. Analysis of velocity and density profile measurements from Station B90 and the nearby Station B75 suggest that anticyclonic eddies and near-inertial waves can interact in these coastal waters to produce significant horizontal advective density fluxes in the pycnocline.

© 2011 Elsevier Ltd. All rights reserved.

1. Introduction

Turbulent mixing in the upper ocean is important to many aspects of oceanography, such as air-sea interactions and near-surface properties, as well as practical applications such as search and rescue and oil spill tracking. Yet, turbulence measurements are not carried out routinely in oceanographic surveys, and even when they are made, they are not often done in concert with auxiliary measurements necessary for interpretation of turbulence properties. Thus, datasets which contain measurements of on-site meteorological parameters and of ocean currents together with microstructure profiles provide valuable case studies of one dimensional mixing budgets and help to improve our understanding of turbulent mixing parameterizations.

As part of the Naval Research Laboratory/NATO Undersea Research Center (NRL/NURC) Dynamics of the Adriatic in Real

Time (DART) Project, we performed turbulence measurements in the upper layers of the Adriatic Sea during DART 06A (see Carniel et al., 2008) and 06B cruises in late March and August of 2006, respectively. We were able to deploy a turbulence microstructure profiler from the NATO RV Alliance and measure the dissipation rates of Turbulent Kinetic Energy (TKE) and temperature variance, and infer eddy diffusivities in the water column. Nearly, 500 profiles were obtained, 300 of them during the DART 06B cruise of which 163 were made at a single station outside the Gulf of Manfredonia in the Southern Adriatic Sea under a variety of environmental conditions. This station was selected for turbulence measurement focus as it provided the maximum amount of auxiliary observational data for interpretation.

There has been an upsurge of interest in recent years in the Adriatic Sea: Dynamics of Localized Currents and Eddy Variability in the Adriatic (DOLCEVITA: Lee et al., 2005), Adriatic Circulation Experiment (ACE: Book et al., 2007), and ADRIA01-03 carried out in the early 2000s in the northern Adriatic, and the Joint Research Project undertaken by NRL, NURC, and other partners in the southern Adriatic under the DART-06 campaigns. Although each of these campaigns had diverse and multiple focuses, several have included direct measurements of the turbulent properties of the

* Corresponding author. Tel.: +39 041 2407956.
E-mail address: sandro.carniel@ismar.cnr.it (S. Carniel).

¹ Fax: +39 041 2407956.

² Fax: +1 303 4928285.

³ Fax: +49 39932/13216.

Adriatic Sea (Peters and Orlic, 2005, Peters et al., 2007, Carniel et al., 2008, and this study). As part of DART, several moorings were deployed in the coastal waters around the Gulf of Manfredonia (see Fig. 1). These included moorings capable of measuring the velocity structure in the water column using upward-looking ADCPs deployed in trawl-resistant bottom mounts. Many of these were the relatively new SEPTR moorings, which also had profilers and sensors to measure water column properties as well as meteorological and wave conditions (Book et al., 2008). One such mooring was deployed at Station B90 (41.67°N, 16.60°E) in 90 m deep waters east of Manfredonia, close to the Western Adriatic Current (WAC) frontal system. During the August 2006 DART 06B

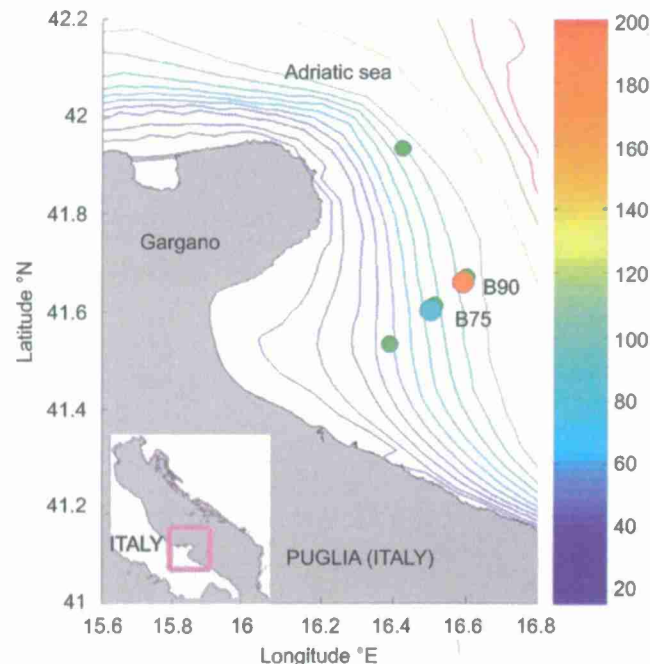


Fig. 1. Station B90 (red circle) was where microstructure observations were made near moorings deployed under the NRL/NURC DART068 campaign. Station B75 is indicated by a cyan circle. SEPTR buoy are represented with green circles. (For interpretation of the reference to color in this figure legend the reader is referred to the web version of this article.)

cruise, we spent considerable amount of time in the immediate vicinity of B90 (Fig. 1) making microstructure measurements (Table 1) in the upper layers of the water column.

We were able to measure turbulent mixing in the summertime strongly stably stratified water column under a variety of meteorological forcing conditions. In this paper, with the help of the meteorological measurements made by the NRV Alliance and other data collected there, we describe the turbulence and mixing properties that characterized the conditions at B90. These measurements highlight the natural variability that characterizes these kinds of observations over various atmospheric forcing conditions. Additionally, the adjacent mooring, SEPTR B75, was used together with SEPTR B90 to make a first estimate of some factors affecting the three dimensional mixing budget of this coastal frontal system.

2. Measurements framework

Microstructure measurements were carried out from August 21, 13.09 UTC, to August 26, 15.13 UTC in 6 Observation Periods (OPs, see Table 1, indicating also the number of profiles during each experiments). The microstructure profiler used was the MSS 90 L, an advanced version of that described by Prandke et al. (2000) for simultaneous precision measurements of microstructure and physical parameters in marine and limnic water. The suite of sensors consisted of two shear probes for turbulence measurements, a thermistor for temperature microstructure, a precision CTD and a turbidity probe. The profiler was also equipped with a vibration control sensor, a two-component tilt sensor and a water surface detection sensor. The sampling rate for all sensors was 1024 samples per second; the resolution was 16 bit. All sensors were mounted at the measuring head of the profiler, the microstructure ones being placed about 150 mm in front of the CTD sensors. Simultaneous measurements of micro-scale temperature and velocity shear enables turbulence dissipation rates and diffusivities to be inferred (see Appendix A for details and Fig. A1, representing a sketch of the apparatus used).

The profiler was balanced with negative buoyancy, which gave it a sinking velocity of about 0.6 m s^{-1} , and was operated via a dedicated winch, with disturbing effects caused by cable tension (vibrations) and the ship's movement isolated by sufficient slack in the cable to ensure free fall. All MSS measurements were carried out from the most forward point on the bow of NRV

Table 1
List of microstructure measurements at Station B90 during the DART068 cruise.

Station	Date and time (UTC)		Names of micro-structure profiles	Number of profiles	Notes
	Lat °N, Long °E (from-to)	Begin			
OP-1 41.6788, 16.6013 41.6876, 16.6399	2006-August-21 13.09	2006-August-21 15.26	D06B0081 D06B0119	39	Water depth 90 m, low wind speed
OP-2 41.6770, 16.6000 41.6222, 16.6333	2006-August-21 17.03	2006-August-21 18.48	D06B0120 D06B0143	24	Water depth 90 m, high wind speed
OP-3 41.6773, 16.6002 41.6610, 16.6320	2006-August-22 23.29	2006-August-23 02.17	D06B0164 D06B0203	40	Water depth 90 m, light wind, clear sky
OP-4 41.6786, 16.6016 41.6671, 16.6597	2006-August-24 22.31	2006-August-25 01.05	D06B0239 D06B0270	32	Water depth 90 m, moderate to strong wind, clear sky
OP-5 41.6677, 16.5920 41.6389, 16.5969	2006-August-26 13.08	2006-August-26 14.40	D06B0271 D06B0292	22	Water depth 90 m, light wind, increasing, clear sky
OP-6 41.6375, 16.5976 41.6292, 16.6000	2006-August-26 14.45	2006-August-26 15.13	D06B0293 D06B0298	6	Water depth 90 m, high wind, clear sky

Alliance while the ship drifted freely under the influence of the prevailing winds and currents. This enabled the profiler to sample ambient water masses free from the turbulence wake generated by the submerged part of the drifting ship itself, therefore allowing for measurements as close as 2 m from the sea surface. Depending on depth, the measurement interval was between 3 and 5 min. The raw data from the MSS profiler were directly transmitted to the on-board unit of the measuring system, and then to a notebook for data registration. After the data collection was completed, each profile was examined and edited manually, and then processed on-board to infer turbulence dissipation rates and diffusivities.

Besides microstructure measurements, a number of auxiliary data was acquired in the proximity of the B90 station, both in the atmosphere and in the ocean. On the atmospheric side, two meteo stations were operating on-board the NRV *Alliance*, located on the forward mast at a height of approximately 23 m above the sea surface. The units were carrying two sensors for the wind speed (ms^{-1}) and direction (degrees), air temperature ($^{\circ}\text{C}$), barometric pressure (mbar) and relative humidity, and one sensor for solar irradiance (W m^{-2}). Sampling rate was 30 s, and in this paper we will be using 60 s averages for computing the associated heat fluxes.

During the period of observations, some remote sensing products were acquired and processed by CNR-ISAC Rome: Sea Surface Temperature (SST) fields from Advanced Very High Resolution Radiometer (AVHRR) and the surface chlorophyll concentrations from MODIS Aqua. Considering the trade-off between uncontaminated images and frequency of observations, the most useful products turned out to be the daily averaged composite images of SST and the instantaneous chlorophyll maps.

Several instruments deployed around B90 provided useful data to complement microstructure measurements. A wave rider (from NURC) was operating during all the concurrent periods of turbulence measurements in the proximity of the station (41.68°N ,

16.59°E), providing values of significant wave heights and periods. The SEPTR buoy (from NRL) provided full water column profiles of temperature and salinity every 6 h via a winched CTD buoy. This low sampling rate, as dictated by the mooring deployment time and battery duration, provided only twenty water-column profiles from the start of the first OP to the end of the last OP, and therefore was not sufficient to allow us to reconstruct high frequency processes during the period of turbulence measurements. However, a string of 16 thermistors (from NURC) was also moored at B90, with a vertical spacing of 5 m starting from the upper one positioned at 10 m depth, and with a sampling rate of 3 min (see Section 3.2). The SEPTR buoy was also equipped with an ADCP working at 300 kHz, which covered the water column in a burst mode every 15 min during the OPs. The bin size was 1 m, with the first useful bin located 8 m below the surface. Besides providing high-resolution velocity measurements, an additional benefit of the four SEPTRs (see green dots in Fig. 1 for their location) was that they made synoptic measurements of water-column currents, temperatures, and salinities at all measurement sites, allowing estimates of horizontal gradients for these properties.

3. Observations

3.1. Meteorological conditions

Fig. 2 shows the meteorological conditions at Station B90 during the six OPs as determined from shipboard sensors described in the Introduction. The top panel represents the air and sea surface temperatures, the middle one the wind speed and the bottom one the relative humidity.

Fig. 3 (top panel) shows the heat fluxes (W/m^2) during the campaign. The net short wave radiation has been estimated using

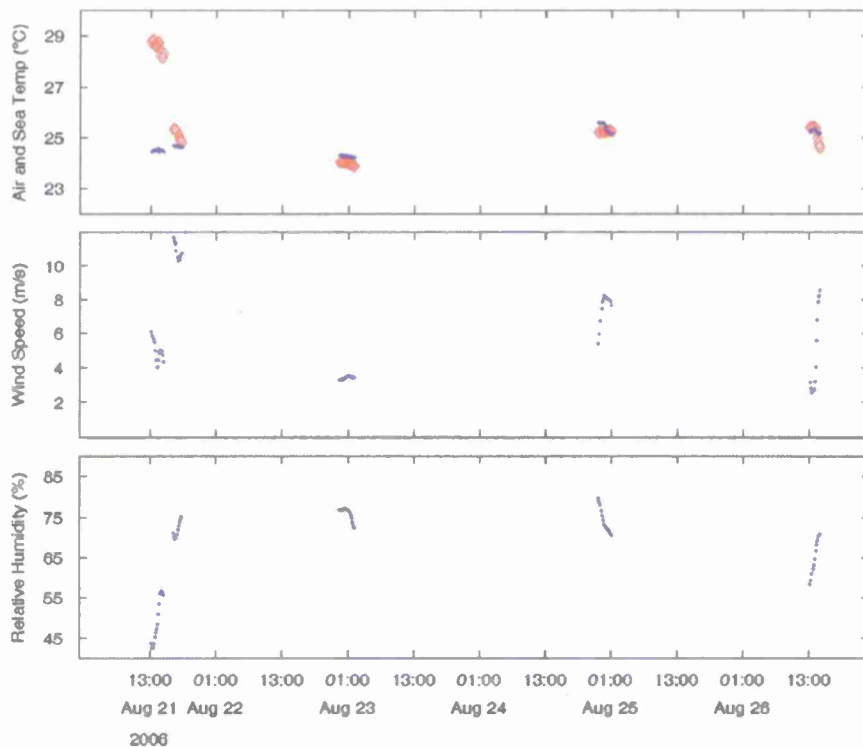


Fig. 2. Meteorological conditions during the six observational periods of microstructure measurements at Station B90 in the southern Adriatic Sea during late August 2006. Proceeding from left to right, OP-1, OP-2, OP-3, OP-4 and OP-5/6. In the top panel red dots denote air temperature and the blue dots SST. Data were acquired by the meteo stations on the NRV *Alliance*. (For interpretation of the reference to color in this figure legend the reader is referred to the web version of this article.)

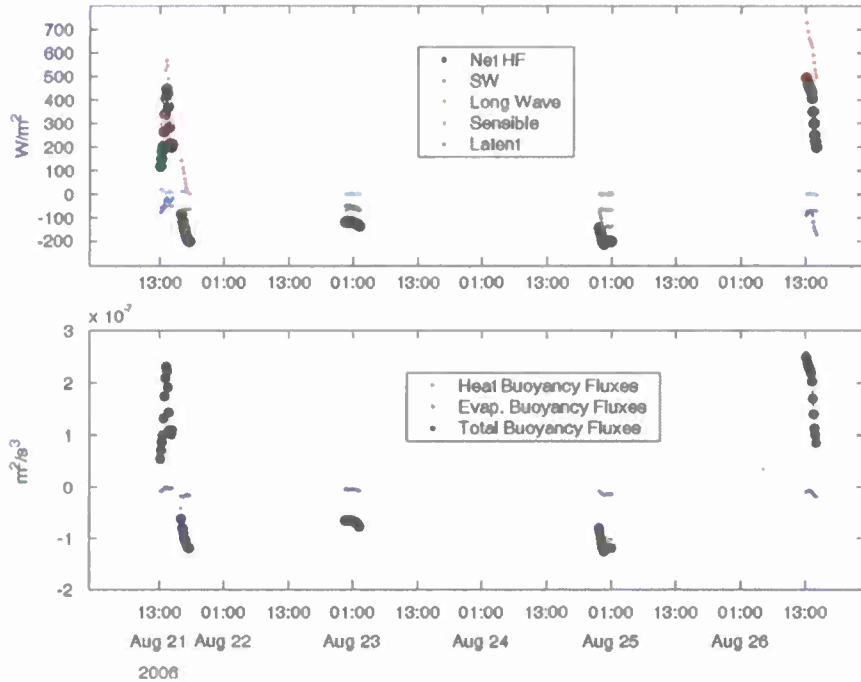


Fig. 3. Heat (top panel) and buoyancy fluxes (bottom panel) at the sea surface during the 6 observational periods of microstructure measurements at Station B90. Proceeding from left to right: OP-1, OP-2, OP-3, OP-4 and OP-5/6. (For interpretation of the reference to color in this figure legend the reader is referred to the web version of this article.)

incoming short wave radiation measurements and the albedo following Payne (1972), while the net long wave radiation using Berliand's formula (see Budiko, 1974 for details) and turbulent fluxes (sensible, latent) following Fairall et al. (1996) formulation. The (bulk) sea surface temperature used in these computations is the uppermost temperature measured by the MSS (roughly 2 m depth).

Fig. 3 (bottom panel) presents the resulting buoyancy fluxes at the surface. The average buoyancy fluxes at the surface are given by $J_{bo} = ((\alpha \cdot g \cdot H_{net})/(\rho \cdot C_p)) + ((\beta \cdot g \cdot S \cdot H_{lat})/(\rho \cdot \lambda_e))$. The first term of the right hand side represent the heat buoyancy fluxes ($\alpha = 0.216 \times 10^{-3} \text{ }^{\circ}\text{C}^{-1}$ is the thermal expansion coefficient, g is the gravity acceleration, H_{net} is the net heat flux, ρ is the reference value for density, 1026 kg/m^3 , and $C_p = 3.98 \times 10^3 \text{ J kg}^{-1} \text{ }^{\circ}\text{C}^{-1}$ is the specific heat of seawater at constant pressure), shown in Fig. 3 (bottom panel) as red dots. The second term of the right hand side are the evaporative buoyancy fluxes (where $\beta = 0.77 \times 10^{-3} \text{ PSU}^{-1}$, S is the surface salinity, H_{lat} is the latent heat flux and λ_e latent heat of vaporization; they are shown in the same panel as blue dots). The latter are much smaller than those due to the heat fluxes at the surface, and therefore the sum J_{bo} reflects mostly the heat buoyancy fluxes. There was no precipitation, and therefore we could not measure turbulence properties under the stabilizing influence of rain. Evaporation rates were also assumed to be small and the effect of the net salt flux on the density structure was ignored. Therefore, any change in salinity seen during the measurement period is assumed to be either due to entrainment or the ship drifting through regions of different salinities.

Fig. 4 (top panel) shows the values of friction velocity u_* (cm/s, defined as $\sqrt{\tau/\rho}$, where τ is the wind stress obtained from data and ρ is the water density) and convection velocity scale $w_* = (J_{bo}D)^{1/3}$ (defined in case of convective situations, where J_{bo} is the average surface buoyancy flux and D is the mixed layer depth, calculated using a temperature-gradient based algorithm). The bottom panel of Fig. 4 shows the Monin–Obukhov length scale $L = u_*^3/(\kappa J_{bo})$, the height above which convectively driven

turbulence dominates over mechanically driven turbulence (note that L is negative if the buoyancy flux corresponds to heat losses, opposite to that of Lombardo and Gregg, 1989, LG89 henceforth, who employ the atmospheric convention for the heat fluxes, i.e., L is positive in case of heat losses).

The effective turbulence velocity scale depends on both the friction velocity u_* and the convective velocity scale w_* ; their relative magnitude, expressed by $R = (w_*/u_*)^3$, determines whether the wind stress or the buoyancy flux dominates turbulence production (see Fig. 4, bottom panel). When $R < 1$, then shear-generated turbulence dominates the Mixed Layer (ML) as a whole; when $R > 1$, turbulence in the bulk of the ML is convection-driven (Kantha, 1995).

Microstructure measurements were made for a few hours on the 21st, 22nd, 25th and 26th of August at B90. Because of the late summertime conditions, there was a strong thermocline and a coincident halocline at a depth of around 15–20 m. The pycnocline was strong with a density change of 2.6 kg m^{-3} within a depth change of 15 m. Under these conditions, the surface-driven turbulence cannot be expected to penetrate much below the upper 15–20 m, and any turbulence in the pycnocline is most likely related to shear instabilities or horizontal mixing processes. Below the pycnocline, one can expect low levels of turbulence and mixing and indeed, below about 35–40 m, the background dissipation rate seldom exceeded $10^{-9} \text{ W kg}^{-1}$. We did not make turbulence measurements in the bottom boundary layer of the water column.

3.2. Hydrological conditions

Temperature profiles provided by the thermistor string, and winds from the meteorological model maintained by the COSMO consortium (www.cosmo-model.org) operating at a resolution $7 \times 7 \text{ km}$, Signell et al., 2005) at the B90 location are plotted in Fig. 5. The black dots represent the times when the ship was

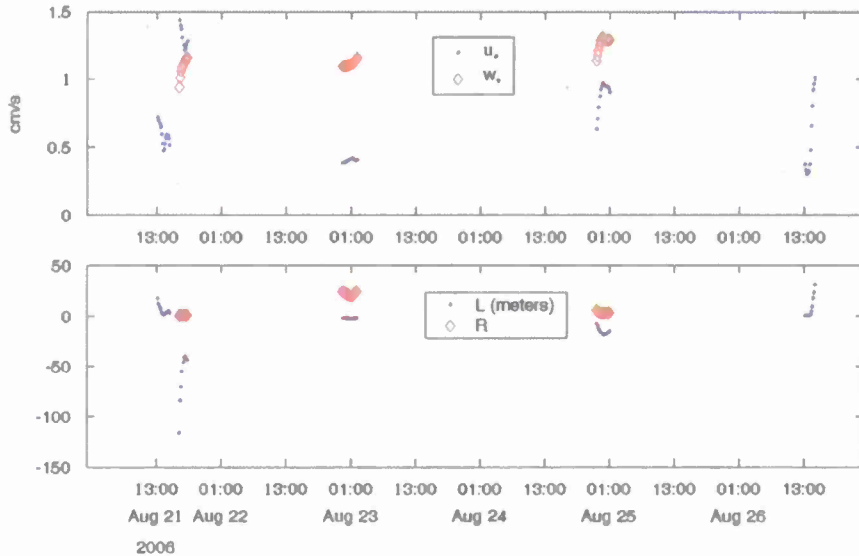


Fig. 4. Friction velocity u_* and convective velocity scale w_* (cm/s, top panel); Monin-Obukhov length scale (L , meters) and the non-dimensional ratio $R = (w_*/u_*)^3$ (bottom panel) during the 6 observational periods of microstructure measurements at Station B90. The OPs are from left to right OP-1, OP-2, OP-3, OP-4 and OP-5/6.

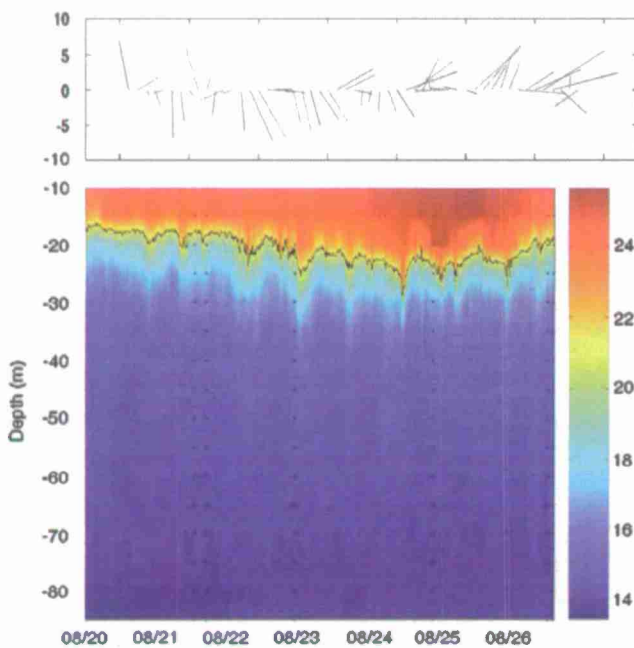


Fig. 5. Temperature evolution at Station B90 as observed by the string of 16 thermistors deployed near the SEPTR mooring during the 6 OPs of turbulence measurements (black dots) and associated thermocline depth (21°C isotherm given as a dashed line). Data were sampled every 3 min and plotted unfiltered. The upper panel presents the wind direction and magnitude (m/s, max. value 11 m/s) from the meteorological model COSMO at a model gridpoint nearby Station B90 (data every 3 h).

repositioned to be at the station before starting each of the 6 OPs of turbulence measurements. Overall, the ML depth was relatively constant during the 6 days of turbulence measurements. OP-1 and OP-2 were characterized by a shallower thermocline, around 18 m, that deepened to about 25 m during OP-3, as a consequence of a rather energetic wind event. Despite a general tendency of warming in the very upper layers during the following days, OP-4 had a ML depth of about 20 m, while during OP-5 and OP-6 the ML depth was again somewhat shallower. ML depth variations in

this region are not only due to local one-dimensional processes but are strongly affected by the mesoscale dynamics of the WAC frontal system (Burridge et al., 2009). Below the upper 35 m, the conditions remained relatively unchanged throughout the OPs.

An analysis of the available satellite images (not shown) shows the general surface conditions in the region surrounding Station B90. At the start of the OPs, the region was characterized by complex fronts, with surface water masses having temperatures between 25 and 25.5 °C south of Gargano promontory and to the west of B90, slightly warmer than and separated from the offshore colder waters. Surface temperature was relatively constant from 21st to 23rd, but a general warming of the ocean surface occurred on August 24th becoming more evident on the 25th with temperatures increasing to 27 °C. Even though the SSTs were roughly 1.5 °C higher, the water mass structures were very similar to those characterizing the situation during August 21st to 23rd, with warmer masses in the west, colder ones to the east, and the station still located in the region of frontal activity. Some further descriptions of the details of the frontal and mesoscale eddy dynamics of this region can be found in Burridge et al. (2009), Magaldi et al. (2010) and Taillandier et al. (2008).

The array of moored observations shows the general mesoscale conditions prevailing at Station B90 during the OPs. ADCP measurements at Station B90 itself (Fig. 6) show general flow in the mixed layer towards the southeast (along-shore WAC direction), punctuated at the beginning of the OPs by alternating pulses of positive and negative velocities in both velocity components. As shown by an inertial band-pass filter of the velocities, (Fig. 6, bottom panel) these clockwise rotating currents are near-inertial internal waves with a characteristic phase reversal at the thermocline and were particularly strong in the first 3 OPs, i.e., from August 20th to 24th. After the latter date, near-inertial oscillations were much reduced in the mixed layer, but increased to a new maximum at the depth level of the pycnocline where inertial velocities were previously at a minimum (Fig. 6, bottom panel). B90 and other ADCP observations show that the station was generally located in the offshore side of an anticyclonic eddy (e.g., see Fig. 2a of Burridge et al., 2009) during the OPs. The negative relative vorticity at B90 from this eddy increased after OP-3, and the pycnocline maximum of near-inertial energy followed this increase after about one inertial cycle. This is

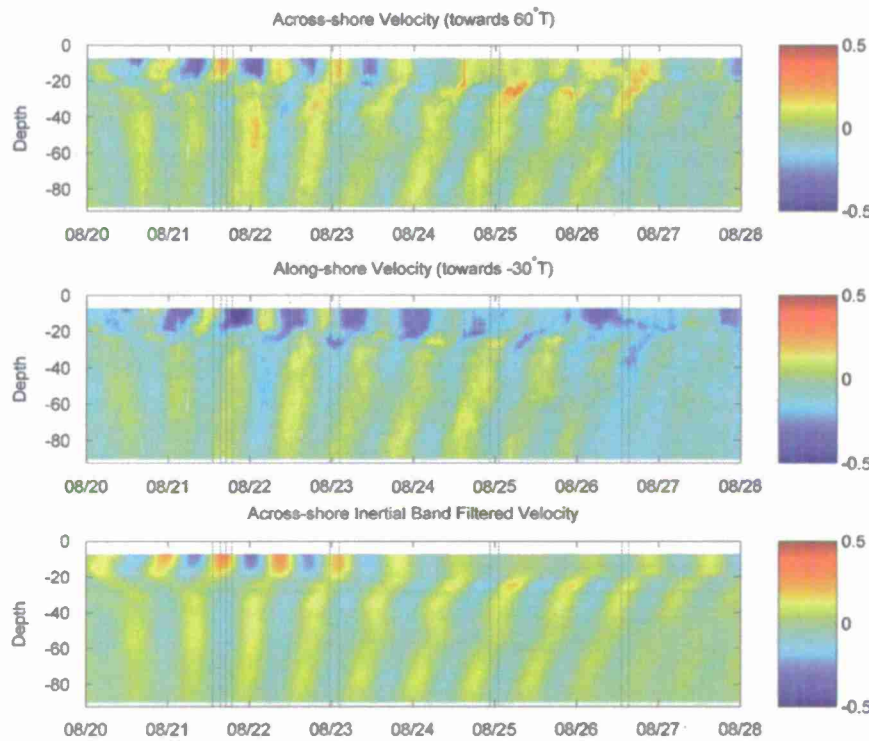


Fig. 6. Across-shore (top panel) and along-shore (middle panel) components of velocity (m/s) in the water column at Station B90 during the study period, as determined from ADCP measurements. The bottom panel additionally shows the near-inertial band (filtered by a 4th order band-pass Butterworth filter ran forwards and backwards with cutoff frequencies of 1.2 and 1.9 cycles per day) component of the across-shore flow. The gray dotted vertical lines denote the starts and ends of the different OPs of microstructure measurements.

suggestive of the process of stalling and trapping of near-inertial waves with frequencies below Coriolis at the base of a region of negative vorticity such as an eddy or ring as described in Kunze et al. (1995) and previous works.

To further test this hypothesis, we computed the across-shore relative vorticity component from low-pass filtered (28 h cutoff) velocities measured at stations B90 and B75, and used the complex demodulation procedure described in Hebert and Moum (1994) to estimate the amplitude and frequency of near-inertial waves at different depths and for specific time periods. Consistently from OP-3 to OP-6 the upper 20 m of the water column had across-shore relative vorticities near -0.1 times Coriolis allowing near-inertial waves to travel downward to the base of this region of negative vorticity. The hypothesis of stalling near-inertial waves at the base of the anticyclone is further supported by the complex demodulation analysis as the results show a 20.2 cm/s amplitude near-inertial wave at 15 m depth over the period August 21–24 decaying in amplitude to 6.0 cm/s over the period August 24–27 while at the same time the amplitude at 25 m grows from 7.2 to 13.7 cm/s. At 15 m for August 21–24 and at 25 m for August 24–27, both near-inertial waves are found to have frequencies of 1.035 times the inertial frequency with respect to a stationary observer.

The velocity shears in both directions (not shown) indicate a maximum in the thermocline region (15–25 m), the region deepening slightly during the OPs. Almost all of the shear maximum can be attributed to the effect of the near-inertial oscillations, which force a phase reversal at the thermocline during OPs 1–3 and have a velocity maximum near the thermocline for OPs 4–6. From the B90 ADCP velocities and the Brunt–Vaisala frequencies computed from the MSS profiler data, we computed gradient Richardson numbers $Ri = N^2 / ((dU/dz)^2 + (dV/dz)^2)$ in the water column during the various

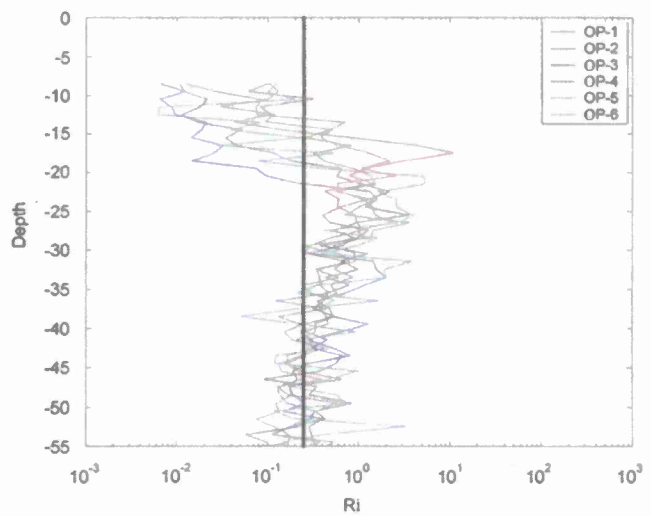


Fig. 7. The median gradient Richardson number profiles in the water column at Station B90 during the different observational periods, as determined from ADCP and MSS measurements. The thick line corresponds to Ri value of 0.25.

OPs. The median values are shown in Fig. 7, where the thick line corresponds to Ri value of 0.25 and OP-5 and OP-6 have been grouped together. The median is a better representative of a typical Ri profile than the mean because Ri can become very large in a few instances when the shear is near zero and these values skew the mean towards larger values. It can be seen that in the ML, Ri is usually much less than 0.25, while in the pycnocline region and slightly below that depth, Ri is usually much higher than 0.25 (note the logarithmic scale). In the lower water column,

the median Ri remains close to 0.25 and individual profile values frequently fall below that value during all the OPs.

To further analyze the Ri results, the velocity shear was divided into different components and Ri profiles, and medians were calculated (not shown) using certain frequency bands of velocity shear rather than the total velocity shear which is used in Fig. 7. Our tests show that low Ri values were not usually produced by the low frequency components (low-pass filter with 28 h cutoff) of the flows, near-inertial band components (band-pass filter with cutoffs at 12.6 and 20 h), or tidal currents (response analysis). Rather, low Ri values in the ML and in the lower water column were generally produced by the high frequency components (high-pass filter with 11 h cutoff) of the flow. Error ensembles were constructed to test sensitivity to noise in the Ri calculation and the qualitative results from the calculation were found to be significantly above the resulting expected uncertainties in Ri median values.

Therefore, it can be concluded that while inertial-band and lower frequency shears were generally not strong enough to produce shear instabilities even in the well mixed regions of the water column, short-time scale shears, presumably linked to small spatial scales, were sufficiently strong at Station B90 during our measurements to produce these instabilities, especially in the surface ML, and could have played a role in turbulent mixing above and below the pycnocline regions.

However, in the pycnocline regions, no velocity shears (including the maximum shears associated with near-inertial waves) were generally strong enough to overcome stabilizing effect of the stratification, and turbulent mixing due to shear instabilities should have been suppressed at these depths during our measurement periods.

In agreement with this finding, preliminary results obtained while integrating the General Ocean Turbulence Model (GOTM) during OP-2 have shown that, when assimilating SEPTR ADCP data via a simple relaxation scheme (nudging), the modeled dissipation rate of the TKE was in better agreement with measurements than the case with no assimilation of velocity data. This was not true when using the NRV Alliance shipboard ADCP data (300 kHz, 4 m depth bin resolution), confirming that the improvement was due to the relatively high vertical resolution of SEPTR ADCP data that enabled the velocity shears to be adequately resolved at small scales.

The wave rider data showed that the wind waves were generally small (e.g. 0.35 m in OP-3 and 0.80 m in OP-5/6), reaching a maximum value of 1.2 m only for a short period during OP-2. The effect of surface waves on mixing was, therefore, ignored.

3.3. Turbulence

Data from the microstructure profiler enabled Thorpe scale L_T , indicative of the turbulence overturning scale, to be determined in addition to ε , the dissipation rate of TKE, χ , the dissipation rate of temperature variance, and the eddy diffusivity K_p and heat diffusivity K_h . Standard sorting procedure was used to determine the Thorpe scale (Thorpe, 1977), calculated from the potential density profiles.

3.3.1. Weak surface forcing (OP-1)

During the early afternoon of August 21st, the wind was moderate with an average value of about 4.9 m s^{-1} ($u_* \sim 0.58 \text{ cm s}^{-1}$), and the solar insolation was such that the net buoyancy flux at the surface was stabilizing with an average heat flux of about 260 W m^{-2} (see Figs. 2 and 3). This caused the turbulence in the upper layers to be very weak as can be seen from the dissipation rates and the

Thorpe scale in Fig. 8, which shows the average profiles with relative bootstrap confidence intervals (bootstrap data samples were 1000 in each analysis). While the pycnocline depth was about 13 m, the Monin–Obukhov length scale L was only 5.2 m so that below this depth, one can expect turbulence to be rather weak.

The pycnocline was strong as indicated by the maximum buoyancy frequency N of about 0.05 s^{-1} . The small Thorpe scale L_T (less than 0.5 m) is indicative of the weak mixing above the pycnocline. The diffusivities K_p and K_h derived from the measured TKE and temperature variance dissipation rates ε and χ were consistent with each other.

3.3.2. Wind-driven turbulence (OP-2)

Towards the evening of August 21st, the winds picked up reaching a maximum speed of 13.1 m s^{-1} at the beginning of the observations, then decreasing to 11.2 m s^{-1} at the end (Figs. 2 and 3), with an average value of around 10.8 m s^{-1} ($u_* \sim 1.29 \text{ cm s}^{-1}$). The net heat flux at the surface reversed so that the ocean cooled with an average heat loss of about -161 W m^{-2} during the 105 min of microstructure profiling. The average buoyancy flux at the surface J_{bo} was $-1.02 \times 10^{-7} \text{ m}^2 \text{s}^{-3}$ and the ML depth 13 m so that $w_* \sim 1.0 \text{ cm s}^{-1}$. The ratio $R \sim -0.6$ indicates that the turbulence was predominantly wind-driven in the bulk of the ML. This is also supported by the large Monin–Obukhov length scale, ~ 58 m, so that D/L (where D is the mixed layer depth) was only 0.22. The Thorpe scales were large in the ML (Fig. 9) reaching a maximum of 2 m indicating strong mixing. Once again, the diffusivities K_p and K_h derived from ε and χ are consistent with each other.

As pointed out by Pollard et al. (1973), the ML results can also be interpreted along the line of reasoning that upon the introduction of a wind stress the upper surface layer deepens until the MLD reaches a value given by $h_{\max} = A_{PRT} (u_* / \sqrt{N_{pc} f})$. A_{PRT} is a constant ($2^{3/4}$ for Pollard et al., 1973), u_* is the friction velocity, N_{pc} is the buoyancy frequency of the layer adjacent to the (surface) ML ($\sim 0.03 \text{ s}^{-1}$ in our case) and f is the Coriolis parameter ($9.66 \times 10^{-5} \text{ s}^{-1}$ at the B90 latitude). Generally speaking, wind stress acts as a source of both internal gravity waves and mixing in the upper ocean; the sharp transition between the acceleration induced in the ML and the stratified region beneath generates relatively strong shears at the base of ML, responsible for its continuous deepening. Adopting the simple 1-D parameterization introduced by Pollard et al. (1973) for this OP leads to a value of $h_{\max} \approx 34$ m as maximum expectable depth of the surface ML, that seems a reasonable value compared to the evidence and the approximations (see again Fig. 5). The wind injection that characterized OP-2 is then leading to an erosion (i.e. deepening) of the existing thermocline, the most likely interpretation of the mixing process being due to breaking internal waves. More recent works (Lozovatsky et al., 2005) seem to demonstrate that the highest correlation between the ML depth (both the measured value and the one obtained via h_{\max} computation) and the friction velocity u_* is reached at a time shift of 12 h, being the time lag possibly associated with the spin-up time of inertial oscillations. The same paper proposes a new value for $A_{PRT} = 1.9$, demonstrating that the constant is, at least to some extent, case-dependent. However, since the next observations after OP-2 in the same area were carried out about 30 h later, we are not able to draw more in-depth considerations on this phenomena and we limit our discussion at this level, being its full interpretation beyond the scope of the present article.

3.3.3. Convection-driven turbulence (OP-3)

On the other hand, on August 22nd–23rd, around midnight, winds died down but the clear sky and the warm SST (warmer than the air temperature) led to considerable cooling (Figs. 2

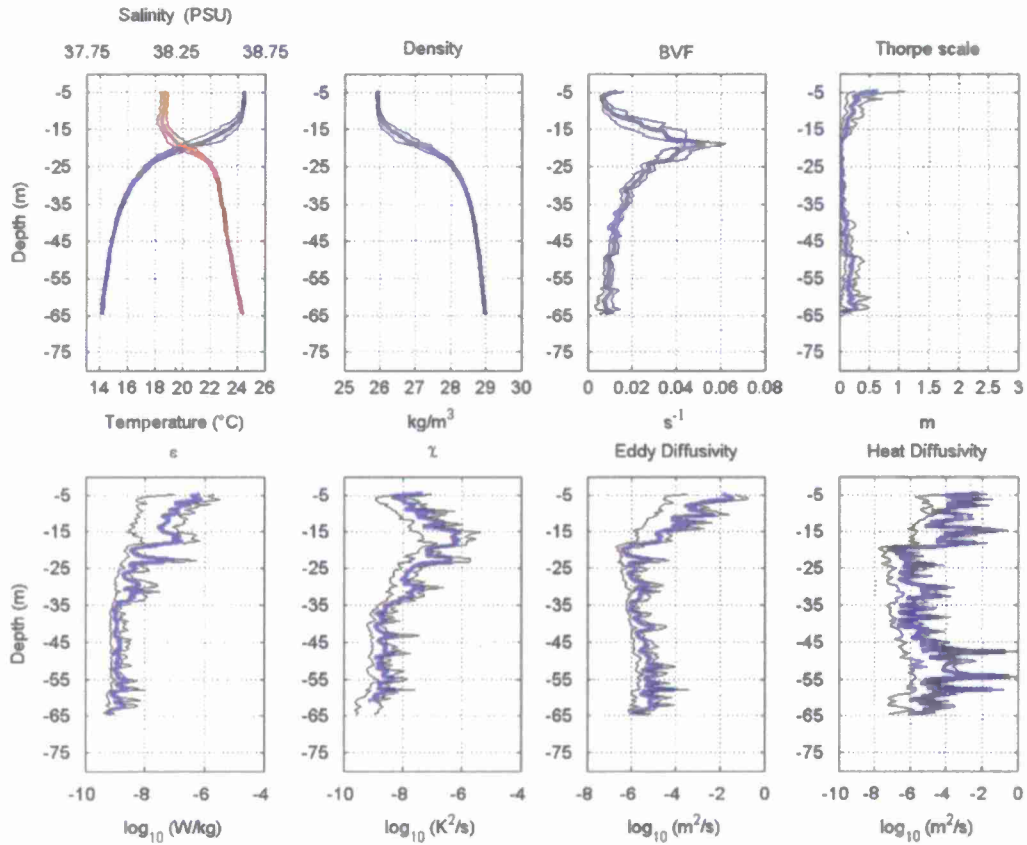


Fig. 8. Profiles of temperature ($^{\circ}\text{C}$) and salinity (PSU, red), density (kg m^{-3}), buoyancy frequency (s^{-1}), and the Thorpe scale (top panels); TKE dissipation rate (W kg^{-1}), temperature variance dissipation rate ($\text{K}^2 \text{s}^{-1}$), eddy diffusivity K_p ($\text{m}^2 \text{s}^{-1}$), and the heat diffusivity K_h ($\text{m}^2 \text{s}^{-1}$) (bottom panels) as measured during OP-1 (see Table 1). The blue line denotes the corresponding mean value, the two thinner lines are the bootstrap confidence limits. Note the small dissipation rates in the mixed layer proper. The slow change in salinity during the OP is due to the ship drifting over a patch of brackish water. (For interpretation of the reference to color in this figure legend the reader is referred to the web version of this article.)

and 3). Fig. 10 shows the dissipation rates and diffusivity coefficients measured during this time. The pycnocline depth was 20 m and the buoyancy flux J_{b0} was $-6.92 \cdot 10^{-8} \text{ m}^2 \text{s}^{-3}$ yielding a value $w_* \sim 1.1 \text{ cm s}^{-1}$. The average wind speed was 3.4 m s^{-1} so that $u_* \sim 0.4 \text{ cm s}^{-1}$ and the ratio $R \sim 21.5$. Clearly, the turbulence in the bulk of the ML was buoyancy-dominated. This is also indicated by the Monin–Obukhov length scale of 2.3 m, much lower than the depth of the ML. The large Thorpe scales (maximum of nearly 3 m) in the ML are indicative of strong convection-driven mixing.

3.3.4. Mixed forcing (OP-4)

During the night of August 24th/25th, around midnight, once again conditions were conducive to night time cooling with an average heat flux of 190 W m^{-2} . However, under moderate winds of 7.2 m s^{-1} (average) and a ML depth of 18 m, $u_* \sim 0.9 \text{ cm s}^{-1}$ and $w_* \sim 1.3 \text{ cm s}^{-1}$ so that $R \sim 3.0$. Turbulence was therefore both convection and wind-driven, with the former somewhat stronger than the latter. Fig. 11 shows the measured dissipation rates and the inferred diffusivities. The large Thorpe scales (maximum of nearly 3 m) in the ML are again indicative of strong mixing.

3.3.5. Turbulence under daytime heating (OP-5/6)

On August 26th, we started microstructure measurements at 13:08 UTC. There was strong solar insolation at that time, and the net heat flux was about 493 W m^{-2} and into the ocean. The

stabilizing heat flux suppressed turbulence, and the light wind at 3.1 m s^{-1} was the primary source of turbulence near the surface. The Monin–Obukhov length scale L was only 1.9 m. But by 14:40 UTC, the winds had picked up to about 6.8 m s^{-1} and the net heat flux had reduced to 300 W m^{-2} so that L increased to 7.3 m. Under these conditions, the turbulence should be confined to a depth of the order of L even though the thermocline/pycnocline was deeper, around 13 m. This is indeed what is observed as can be seen in Fig. 12, which shows the average profiles and the relative bootstrap confidence limits. The dissipation rate below about 5 m depth can be seen to be close to the background level, even though immediately below the pycnocline, turbulence dissipation levels are slightly elevated. The weak nature of turbulence in almost the entire water column is evident from the rather small Thorpe scale in the water column (note that the microstructure measurements are missing in the upper 3 m or so). Slight stable stratification in the ML is also evident in the temperature and density profiles.

The winds continued to increase and the net heat flux continued to decrease in the afternoon so that L had increased to 13.4 m by 14:45 UTC and 21.4 m by 15:15 UTC (OP-6). Wind-generated turbulence was consequently stronger as is evident from the Thorpe scale in Fig. 13, but also penetrated deeper into the ML. The active ML appears to be around 14–15 m, comparable to the average L of 17 m during this period. This lends support to the idea that under a stabilizing buoyancy flux, the turbulent ML depth is proportional to the Monin–Obukhov length scale L .

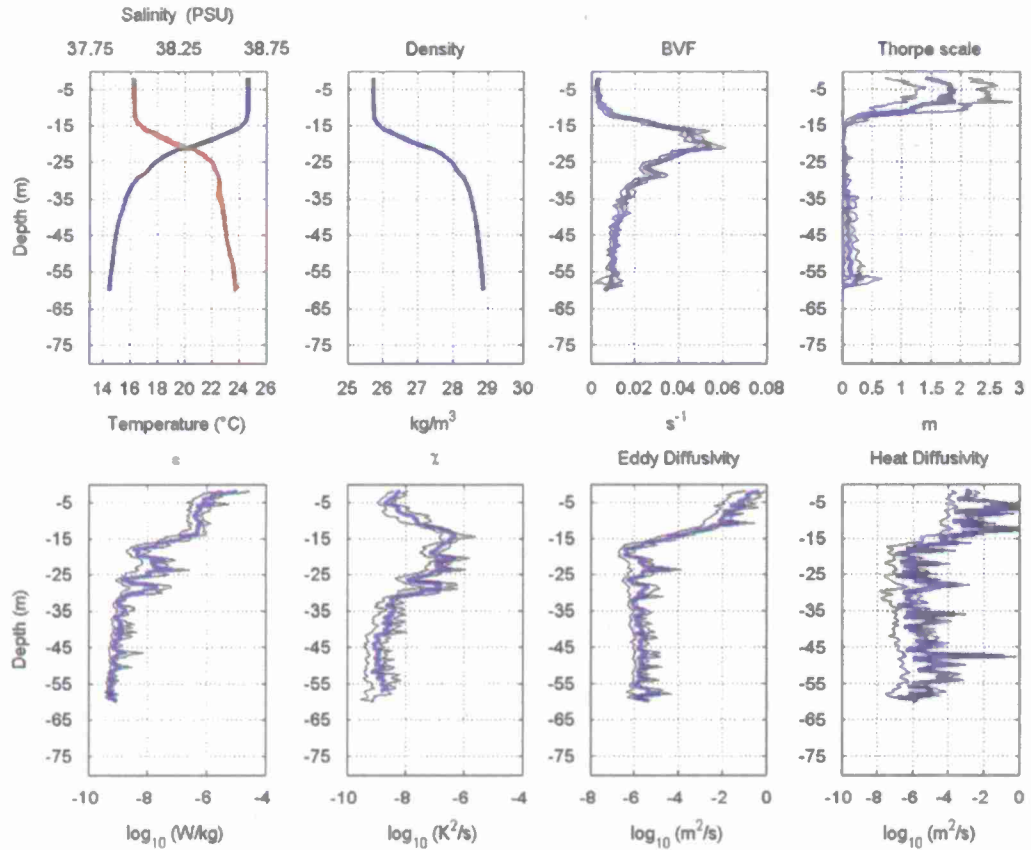


Fig. 9. As in Fig. 8 but for OP-2. Note the strong dissipation rates and the large Thorpe scales in the upper 10 m of the water column due to strong wind forcing.

4. Turbulence scaling

4.1. Turbulence scaling within the Mixed Layer (ML)

Turbulence is generated in the upper ML by the momentum and buoyancy fluxes at the surface. Surface gravity waves also contribute to the TKE budget through wave breaking and Stokes production (Kantha and Clayson, 2004, Kantha et al., 2010). Wave breaking leads to enhanced turbulence levels very near the surface (e.g. Anis and Moum, 1995) and the interaction of the Reynolds stresses due to the wind stress and the shear due to Stokes drift leads to TKE production in the ML (Kantha et al., 2010; Carniel et al., 2005). Since the falling microstructure probe did not allow us to make measurements in the upper 2–3 m, where the influence of surface wave breaking on the TKE dissipation rate would be important, we were not able to account for wave breaking. We did not observe any windrows during daytime when the ambient light enabled us to see the air-sea interface clearly. Neither did we see them during measurements at night, at least in the immediate vicinity of the bow. More importantly, as shown in Section 3, the significant wave heights that were measured were very small. Therefore, we expect the contribution of Stokes production of TKE to turbulent mixing in the shallow ML to be rather small.

When the turbulence in the ML is mechanically driven by the wind stress, away from the surface where turbulence produced by wave breaking is important, the law of the wall prevails, so that the TKE dissipation rate follows the relationship $\varepsilon_S = u_*^3/\kappa z$, where κ is the von Karman constant, u_* is the friction velocity and z is the distance from the surface. This similarity relationship (Dillon

et al., 1981) should hold in the upper layers (below roughly 2–3 m affected by any wave breaking, where microstructure measurements could not be made). The closest analogy to the wind stress-driven ML is Couette flow, except that there is no rigid wall at the bottom of the ML. Unlike for Couette flow where a log law region exists adjacent to the bottom wall, for the wind-stress driven ML a log-law region exists near but away from the surface of the ML and the behavior near the bottom of the ML is rather uncertain. Shear driven mixing is not as efficient as convective mixing and hence the dissipation rate profile is not perfectly uniform. Nevertheless, it is reasonable to assume $\varepsilon_S = c_1(u_*^3/\kappa D)$, where D is the mixed layer depth and c_1 a constant whose value can be determined by matching this outer law to the inner law near the wall. It is well known that in all turbulent boundary layers, the macroscale of turbulence is proportional to the distance from the wall z and, therefore, the dissipation rate varies as the inverse of the distance. We therefore take ε_S in the wind stress-driven mixed layer to be

$$\varepsilon_S = \begin{cases} \frac{u_*^3}{\kappa z} & 0 \leq z \leq 0.3D \\ 3.33 \frac{u_*^3}{\kappa D} & 0.3D < z < D \end{cases} \quad (1)$$

where the value of 3.33 results from matching the above two segments at $z=0.3D$, the value of 0.3 being chosen based on results of laboratory Couette flow experiments (e.g. Tillmark and Alfredsson, 1993 and references cited therein).

Under pure convection, the momentum flux is zero and turbulence is driven solely by buoyancy flux. It is common (Shay and Gregg, 1984, 1986, LC89, Peters et al., 1988, 2007) to assume that the dissipation rate is uniform and equal to $\varepsilon_C = c_2 \cdot J_{bo}$

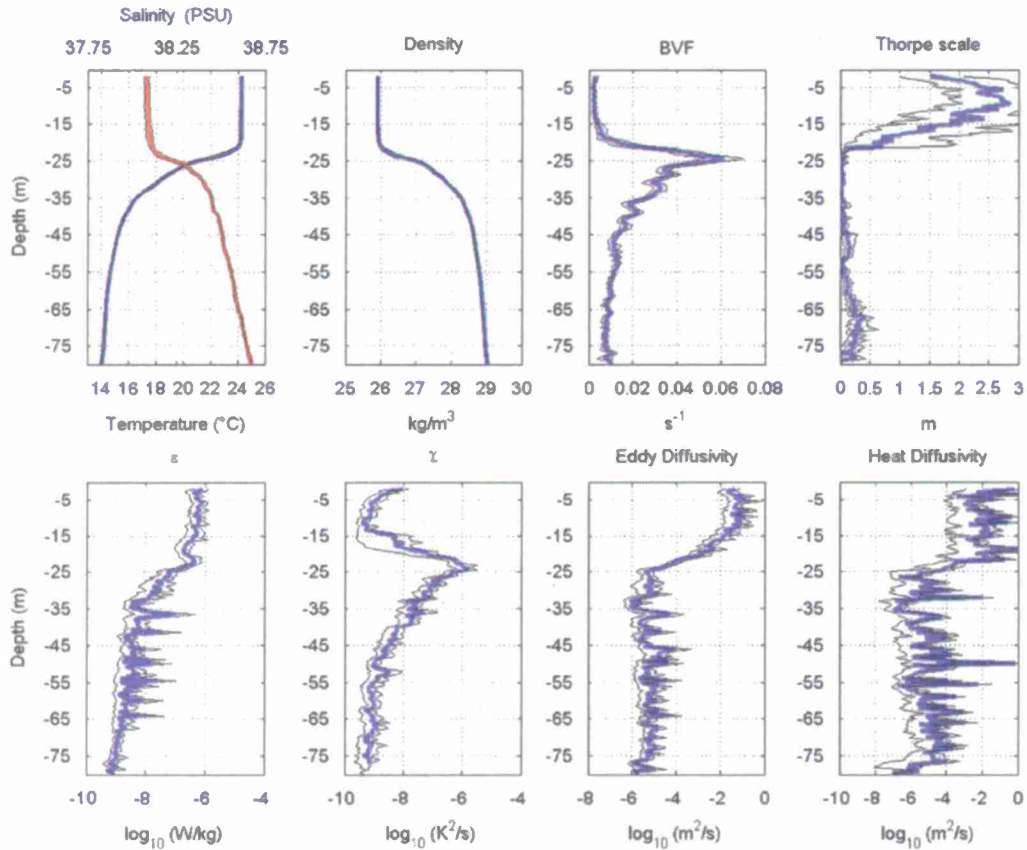


Fig. 10. As in Fig. 8 but for OP-3. Note the strong dissipation rates, large Thorpe scales and the deep ML. The turbulence here is predominantly convection-driven.

in the entire ML. The value of c_2 can be determined as follows. Under equilibrium and quasi-equilibrium conditions, the buoyancy flux in a convective ML is linear, decreasing from J_{b0} at the surface to $-dJ_{b0}$ at the bottom, the negative value resulting from entrainment due to penetrative convection. The integral of the buoyancy flux over the ML, which is indicative of the total production rate of TKE in the convective ML, is therefore $\bar{P} = 0.5(1-d)J_{b0}D$. Since the integral of the dissipation rate of TKE in the ML $\bar{\varepsilon} = c_2 J_{b0}D$ must equal \bar{P} , we get $c_2 = 0.5(1-d)$. The upper bound on d is 0.5 (Kantha, 1980), so that $c_2 = 0.25$. For non-penetrative convection that results when the pycnocline bounding the ML is very strong and the governing Richardson number becomes very large, $d=0$ (Kantha 1980) and therefore $c_2=0.5$. The usual value of d is, however, 0.2 (Kantha 1980), so that $c_2=0.4$. We therefore adopt the following scaling for the TKE dissipation rate in the convective MLs

$$\varepsilon_C = 0.4J_{b0} \quad 0 \leq z \leq D \quad (2)$$

Note that the conventional value for c_2 is 0.58 (e.g. LG89—Eq. (4) below), which is unlikely since the absolute upper bound, as shown above, is 0.5.

For regimes in between when the turbulence is generated by both a momentum flux and a destabilizing buoyancy flux (i.e. $1 < -D/L < 10$), it is reasonable to assume the TKE dissipation rate ε in the ML to be the sum of those due to shear-driven and buoyancy-driven turbulence

$$\varepsilon = \varepsilon_S + \varepsilon_C \quad (3)$$

with ε_S and ε_C given by Eqs. (1) and (2).

Within the ML then, we therefore test the parameterization (3) against the more conventional LG89

$$\varepsilon = \varepsilon_S + \varepsilon_C = 1.76 \frac{u_*^3}{KZ} + 0.58J_{b0} \quad (4)$$

which was also proposed by Brainerd and Gregg (1993a, 1993b) and adopted by Stips et al. (2002). The latter reported results that were in acceptable agreement during periods characterized by daylight stratification, but failed during night-time convection, when the formulation exceeded the measured dissipation rates by a factor of 5. Stips et al. (2002) measurements were carried out in December and were characterized by a general heat loss to the atmosphere, both during day and night-time. This is significant since LG89 proposed their scaling for night-time conditions characterized by convection processes and largest heat losses.

4.2. Turbulence below the Mixed Layer (ML)

In the stably stratified layers in the interior of the water column below the ML, turbulence generation is mainly due to shear-induced instabilities. Therefore, both ε_C and ε_S go to zero, and the relevant length scale is the Ozmidov scale, defined as

$$L_0 = \sqrt{\frac{\varepsilon_I}{N^3}} \quad (5)$$

(where ε_I is the dissipation rate in the interior layers) which is indicative of the maximum size of the eddies (overturbs) in a stably stratified fluid. If an independent estimate of this length

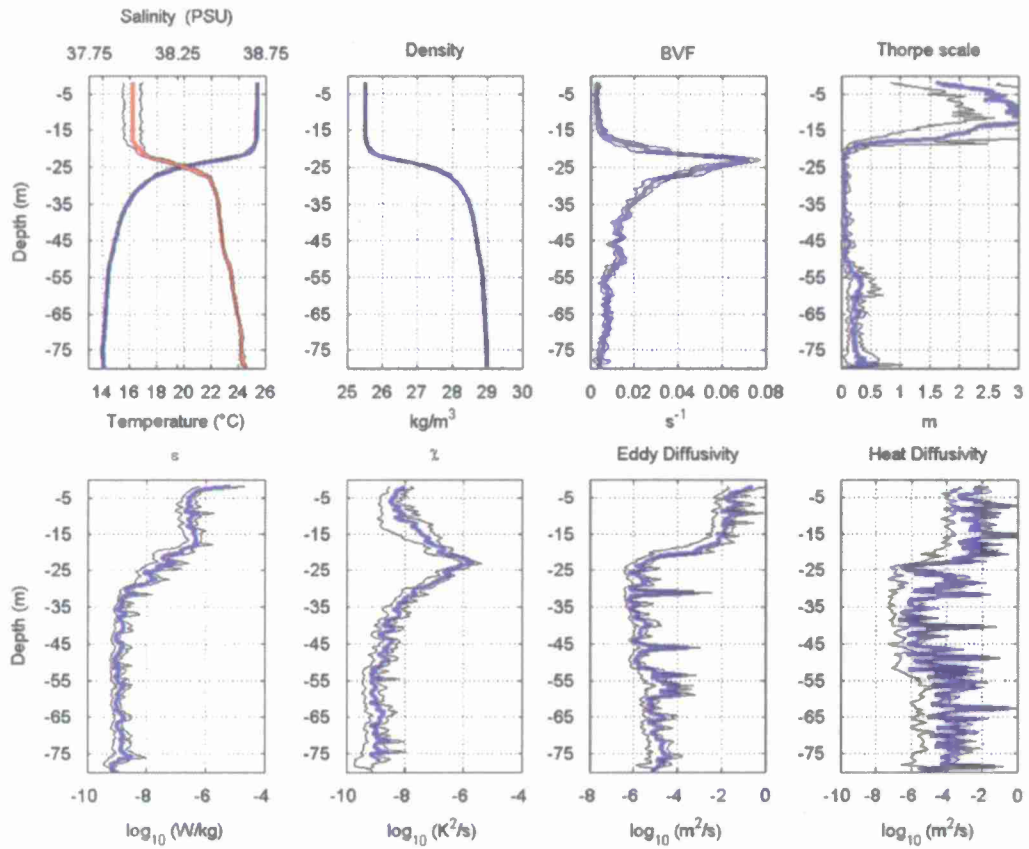


Fig. 11. As in Fig. 8 but for OP-4. During the acquisition there was evidence of a slow decrease in salinity in the mixed layer due to the ship drifting over a brackish patch of water.

scale could be obtained from measurements, the TKE dissipation rate and hence the eddy diffusivity can be inferred.

As mentioned in the previous Section, Thorpe (1977) suggested an elegant method to obtain an estimate of the length scales associated with overturning events in a stably stratified water column, by reordering the observed potential density profiles (which may contain local overturns and hence local regions of unstable stratification) into a stable, monotonic ones. The Thorpe scale L_T is then defined as the root mean square (*rms*) of the resulting displacements, and provides an estimate of the vertical size of the overturns in the water column. Dillon (1982) compared L_T with the Ozmidov scale L_O , and proposed $L_O = 0.79 L_T$, provided the eddies are not too close to the sea surface where they “feel” the boundary, suggesting this distance to be about $10L_O$. By assuming

$$L_O = c_0 L_T \quad (6)$$

an estimate of the overturn scale can be made and this provides an alternative means of inferring the TKE dissipation rate ε in the water column below the ML, provided the background value of local N can also be estimated. The best way to deduce the background value of N is from the sorted monotonic density profile (Dillon, 1982; Thorpe, 2005). Eqs. (5) and (6), lead to

$$\varepsilon_I = C_K L_T^2 N^3 \quad (7)$$

where the coefficient C_K is simply the square of the proportionality constant in Eq. (6). Considerable efforts have been expended in determining the value of c_0 (see Thorpe, 2005 for a summary and Dillon, 1982 for a lucid discussion of the Thorpe scale and related issues). Plots of the observed L_T versus L_O in the ocean show considerable scatter (Osborn, 1980; Dillon, 1982; Wesson and Gregg, 1994; Moum, 1996; Peters et al., 1988; Ferron et al.,

1998; Gargett, 1999; Caldwell, 1983; Galbraith and Kelly, 1996; Fer et al., 2004) typical of all microstructure measurements, and so the value of c_0 does involve some uncertainty. For instance, using aggregated data, Wesson and Gregg (1994) proposed c_0 between 0.25 and 4.0 (and, therefore, C_K from 0.0625 to 16).

There is some debate as to how the overturn scale is to be estimated. Most authors equate it to the Thorpe scale L_T , defined as the *rms* value of the displacements and obtained from binning the displacements and taking the *rms* value in the bin. The length of these bins is not a fixed value (Dillon, 1982) and very often not specified (Wesson and Gregg, 1994). Moreover, some (Dillon, 1982) exclude part of the dataset (data close to the surface or having a very small or zero Thorpe scale) from the analysis that leads to the determination of c_0 .

Generally speaking, in matters involving turbulence, any average quantity is best derived from ensembles. Substituting spatial or temporal averages for ensemble averages is not always valid or desirable. More importantly, since the Ozmidov scale is indicative of the maximum scale of the overturns in a given stably stratified region of buoyancy frequency N , there are reasons to believe that L_T could probably be the ensemble average of the maximum displacements in a given overturning region, rather than the *rms* value of displacements in a bin. However, ensemble averaging requires multiple samples of the same overturning region, which is logically difficult to do, especially given the episodic nature of turbulence. Absence of multiple samples of the same turbulent patch forces one to fall back on a single sample and regard the *rms* value obtained over a pre-selected bin as indicative of L_T . Note also that these concepts are valid only in regions of stable background stratification and therefore a well-mixed upper ML or a convective ML should be excluded.

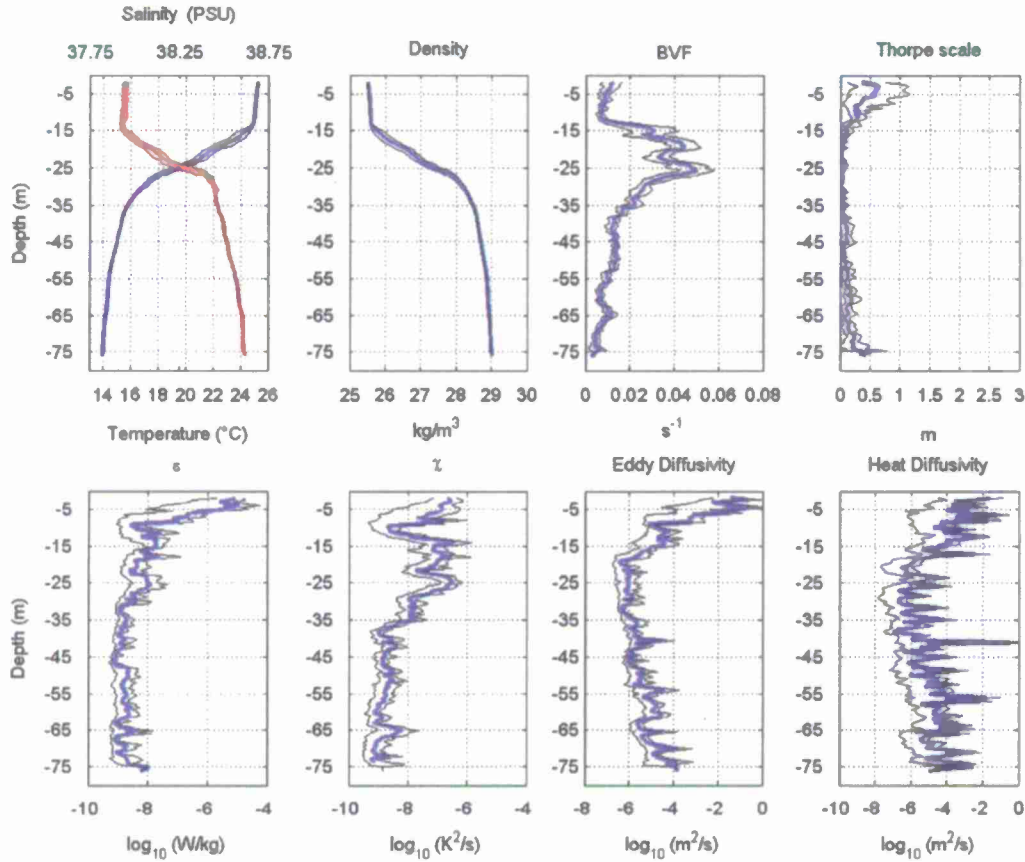


Fig. 12. Same as in Fig. 8 but during OP-5 (see Table 1), under strong solar insolation and weak winds.

To further explore these aspects, we computed the Thorpe scale at different resolutions (0.5 m, 1, 2 and 5 m) using the full dataset available at B90 at all available depths, without distinguishing between different depths. Corresponding values for the proportionality constant c_0 were very similar, ranging from 3.0, 3.1, 3.1 and 3.4, well within the range proposed by Wesson and Gregg (1994). Fig. 14 presents a log–log plot of the values of the L_T versus L_O , for the bin size of 5 m ($c_0=3.4$, correlation coefficient is 0.65). Different color present data bracketing different depths. The limits proposed by Wesson and Gregg (1994) (c_0 between 0.25 and 4.0) are computed following Eq. (6) and shown as black continuous parallel lines. If we use the maximum value of the displacements as indicative of the overturning scales instead of the *rms* value, we find $c_0=2.1$ and a correlation coefficient of 0.65, for the whole dataset and 5 m bin resolution.

However, if we compute the value of c_0 over different depth ranges representative of perhaps different mixing processes, in the upper layers (< 15 m) $c_0=4.1$, in the region bracketing the thermocline (15–30 m) $c_0=1.5$, while in the deeper regions (> 30 m) $c_0=0.3$. If instead we perform our analysis choosing 2 m bin resolution, c_0 values do not change much: 4.2, 0.7 and 0.3. It seems therefore that, at least for this dataset at least, a smaller value for c_0 is appropriate in the deep regions. This value is close to the lower limit of the values reported by Wesson and Gregg (1994) and other investigators.

To sum up, while the approximate proportionality between the overturn scale taken as equal to the Thorpe scale L_T derived from sorting the density profile and the Ozmidov scale L_O is generally accepted as beyond dispute, the value of the proportionality constant remains uncertain. However, as far as turbulence measurements are concerned, our dataset is too limited to

resolve this issue and we conclude that more extensive measurements and careful analyses are needed. For the present study, we will use the value of $c_0=0.3$ ($C_K=0.09$), as determined by the best fit to the dissipation rate profiles below the upper ML at Station B90.

5. Results

We therefore propose that the TKE dissipation rate for the whole water column be parameterized as follows:

$$\varepsilon = \begin{cases} \varepsilon_C + \varepsilon_S & z \leq D \text{ Eq. (3)} \\ \varepsilon_I & z > D \text{ Eq. (7) with } C_K = 0.09 \end{cases} \quad (8)$$

In the following, we focus on the three cases that were either influenced by wind (OP-2), very close to a convection regime (OP-3) or typical of a mixed situation (OP-4), characterized by values for the ratio $-D/L$ of 0.3, 8.6 and 1.2, respectively. We consider only cases with combined convection and wind mixing (OP-2, OP-3, OP-4) since the proposed scaling in the mixed layer is not applicable to cases with stabilizing buoyancy flux at the surface.

Fig. 15 shows the TKE dissipation rate profiles from micro-structure measurements, plotted along with profiles constructed using the LG89 scaling of Eq. (4) (yellow line) and Eq. (8) (black line). Note that the former scaling is valid only within the ML and not below it and therefore we do not extend the yellow line below the ML. A possible explanation for the disagreement between the observations and the theoretical scaling is inaccuracies in inferring J_{bo} and u_* from bulk formulae. It would have been better to actually measure J_{bo} and u_* and we strongly suggest that this be

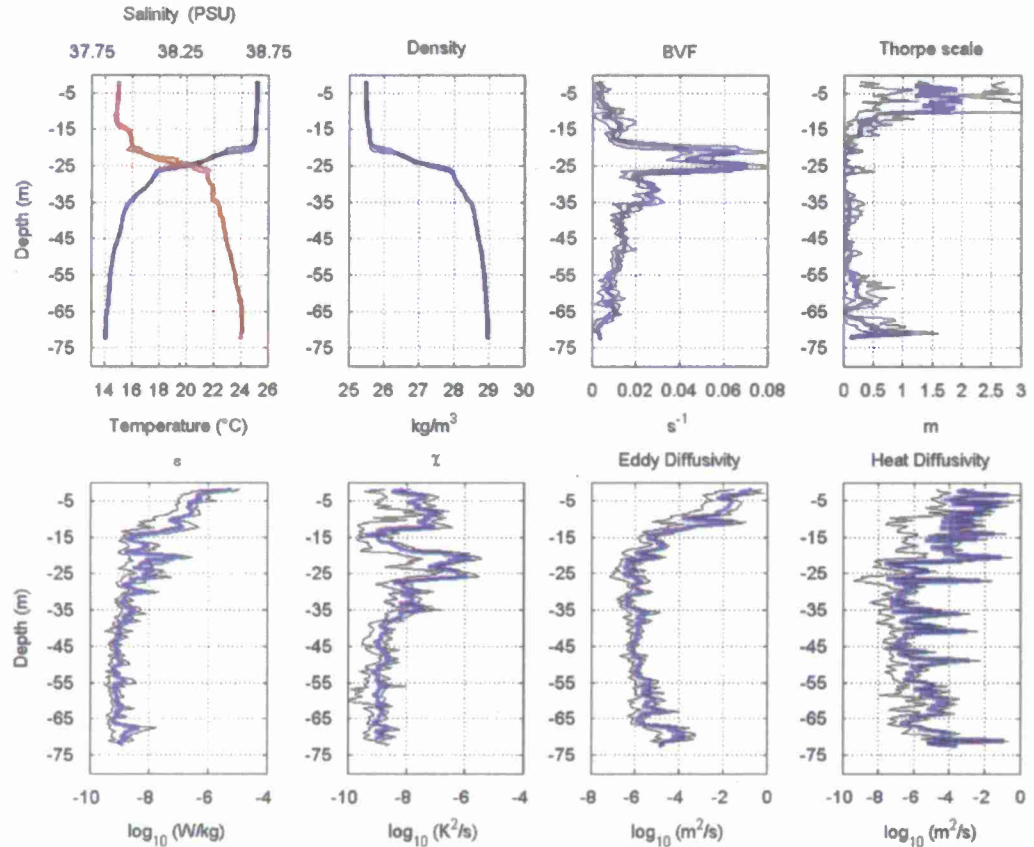


Fig. 13. Same as Fig. 8 but during OP-6, under reduced solar insolation but stronger winds.

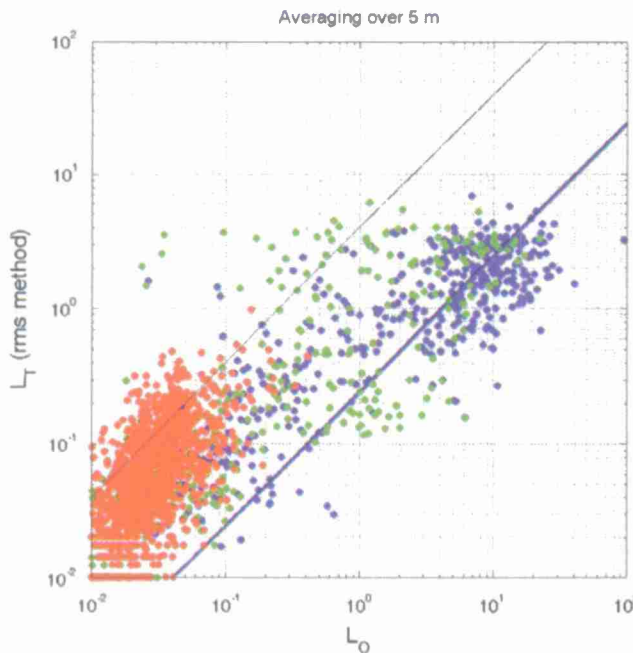


Fig. 14. Plot of L_T versus L_O , using the dataset of the 6 OPs presented in this paper, at 5 m bin resolution. Blue dots: measurements shallower than 15 m; green dots: measurements between 15 and 30 m; red dots: measurements below 30 m. (For interpretation of the reference to color in this figure legend the reader is referred to the web version of this article.)

done in future microstructure studies. As far as the value of the constant adopted for the scaling below the ML, we see that the results are in good agreement with observations when using the suggested value for C_K . Even if we use a larger value for c_0 of 0.77 ($C_K=0.6$), the agreement remains fairly good (note the logarithmic scale). For recent developments, including the issue of noise on identification of overturning regions and extraction of the dissipation rate, see Kantha and Hocking (2011).

The conventional parameterization (yellow line in Fig. 15) was adopted by Stips et al. (2002), who found that the parameterization within the ML was in better agreement during daytime than during night-time. Indeed, during OP-2, characterized by a positive short wave flux, this parameterization compares well (correlation coefficient $r=0.93$) with our measurements. It does not, however, match measurements during OP-3 (performed at night and characterized by strong cooling and convection), where it is smaller by a factor of about 10, with a poor correlation ($r=0.07$). At the same time, in line with what LC89 originally proposed, results for the night-time OP-4 are quite good, characterized by a correlation coefficient $r=0.91$. The alternative parameterization proposed in Eq. (8) (black line in Fig. 15), behaves similarly, with correlation coefficients for the same three cases of 0.78, 0.03 and 0.94 within the ML. When applied to the entire water column, the coefficients become 0.63, 0.14 and 0.56.

Both of the theoretical scalings that were used only consider one dimensional vertical effects, and horizontal variations and advective processes are neglected. However, a portion of the restratification of the ML is unaccounted for by estimates of vertical processes, most likely due to lateral processes (Hosegood et al., 2008). In most studies, lateral effects cannot

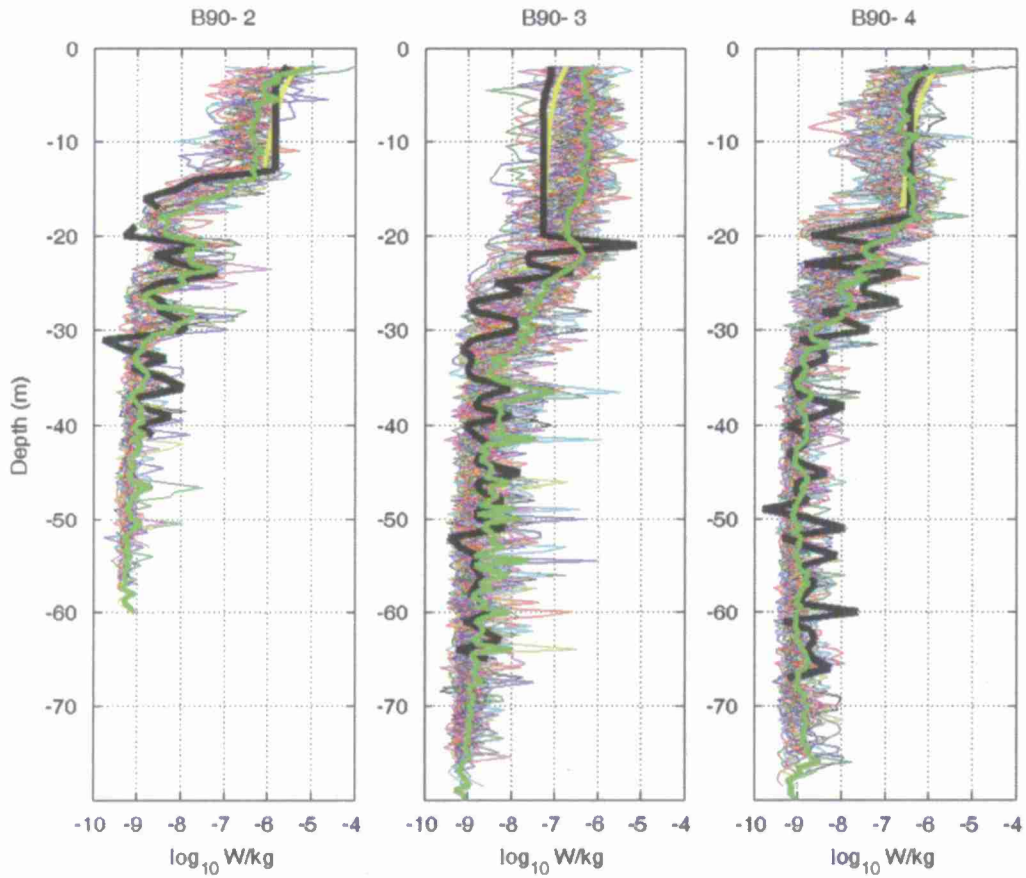


Fig. 15. Observed dissipation rates (the average is in green) compared with theoretical scaling for OP-2, OP-3 and OP-4: yellow line using Eq. (4), black line using Eq. (8). (For Interpretation of the reference to color in this figure legend the reader is referred to the web version of this article.)

be evaluated due to the horizontal point sampling nature of microstructure and CTD probes. However, the DART array with automated, horizontally spaced, synoptically profiling SEPTR moorings provided data on horizontal processes at the same time as vertical processes were measured by the microstructure profiler. Here, we estimate the role of across-shore horizontal advection and mesoscale and inertial stirring at B90 over the 6 h sampling intervals of SEPTR by evaluating the integrated conservation of mass equation for a fixed volume (e.g. see Eq. (7) in Hosegood et al., 2008) using B75 and B90 density profiles to estimate the gradient of potential density, and 6 h low-pass filtered B90 velocity profiles for advection.

$$\Delta\rho_a = \int u_a \frac{\partial\rho}{\partial x} dt \approx \bar{u}_{aB90} \frac{(\rho_{B90} - \rho_{B75})}{\Delta x} \Delta t \quad (9)$$

The results are shown in Fig. 16.

The surface ML and the lower water column are both relatively vertically and horizontally homogeneous in the Station B90 region, and therefore horizontal gradients of density are primarily concentrated in the pycnocline region throughout the OPs. This is illustrated by the two 1027 kg/m³ (representative of the pycnocline) contours plotted in Fig. 16 from Stations B75 and B90, respectively. The inshore site, B75, consistently has a slightly deeper pycnocline depth (as in a geostrophic warm core anticyclonic eddy) and therefore currents at the pycnocline level will flow across the resulting horizontal density gradient and lead to an advective density flux. During OP-1 and OP-2 the advective density flux is small because the velocity minimum of the near-inertial wave is located in the pycnocline (Fig. 6). However, when the velocity maximum of the near-inertial waves relocates to the

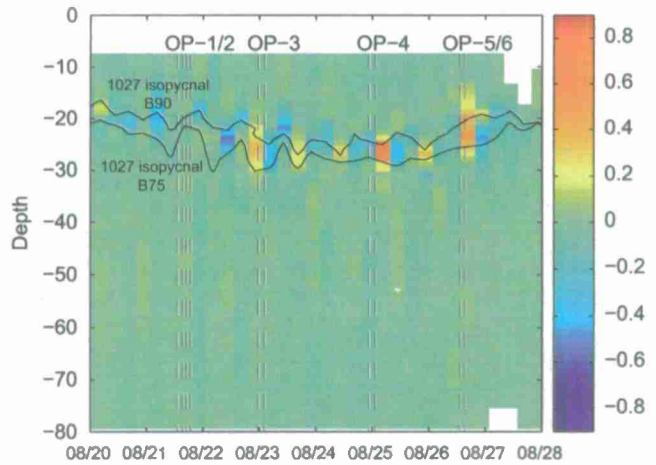


Fig. 16. Potential density change (kg/m³) from horizontal density advection estimated from the integrated conservation of mass equation for a fixed volume (Eq. (7) in Hosegood et al., 2008) using B75 and B90 density profiles to estimate the gradient of potential density, and 6 h low-pass filtered B90 velocity profiles for advection. The 1027 kg/m³ isopycnal contours for B90 and B75 are drawn in black and labeled for reference. The gray dotted vertical lines denote the starts and ends of the different OPs of microstructure measurements.

pycnocline during latter OPs, the advective density flux in the pycnocline can become substantial (Figs. 6 and 16). Therefore, inertial stirring could be an important mixing mechanism at Station B90 near the base of the ML and the pycnocline region

when near-inertial waves become trapped or concentrated there. Further support for this hypothesis can be found in the Aquashuttle observations discussed in Burrage et al. (2009) where salinity and fluorescence anomalies were observed to spread away from minimum/maximum cores along the pycnocline rather than through the ML. The effect of lateral processes seem, therefore, to be confined to the base of the ML.

6. Concluding remarks

During the late August 2006 cruise in the southern Adriatic Sea under the NRL/NURC DART 06B observational campaign, we were able to perform microstructure measurements in the upper layers of a 90 m deep water column in the Gulf of Manfredonia under a variety of meteorological conditions. This has enabled us to look at the turbulence in the upper oceanic ML under strong wind forcing, night-time convection, mixed convection and wind forcing, weak wind forcing and strong insolation. During the study period the ML was shallow between 15 and 25 m. Over 160 profiles were taken providing a rich kaleidoscope of turbulence behavior in a typical strong summertime oceanic thermocline. The TKE dissipation rate measurements in the ML turned out to be consistent with similarity scaling derived from theoretical considerations although there were some disagreements. In the interior, below the ML, the scaling derived from buoyancy frequency and the overturn scale (Eq. (8)) agreed relatively well with observations.

In view of the variability shown during the measurements, it is clear that the availability of high-frequency meteorological forcing and robust turbulence closure schemes are essential to accurate parameterization of sub-grid scale processes. Current numerical models of turbulent mixing, such as GOTM and Kantha and Clayson (2004), are able to model turbulent mixing when provided with an adequately resolved surface forcing and high-resolution velocity shear. Since numerical ocean models of the Adriatic Sea require realistic levels of mixing for accurate depictions of the water mass and current structure in the water column, we believe that turbulence observations such as those presented here need to be carried out more routinely, in order to provide a good comparison database. In this respect, the dataset presented here enhances considerably our previous knowledge of turbulence in the Adriatic Sea gained from roughly 70 microstructure profiles obtained by Peters and Orlic (2005) and Peters et al. (2007) during the DOLCEVITA cruises in 2003, and those described in Carniel et al., 2008.

Finally, the role of horizontal variations and fluxes are often not considered in the interpretation of microstructure measurements. These non-linear processes can be quite complex and involve interactions at various scales, as illustrated by this case where a mesoscale feature (an anticyclonic eddy) both produced a horizontal density gradient and also trapped a near-inertial wave at the base of the mixed layer, all of which served to produce horizontal advective density fluxes in the pycnocline. Further analysis of these processes for the Adriatic and elsewhere are needed.

Acknowledgements

This research was supported by the Office of Naval Research under its NICOP program with grants N00014-05-1-0730 to Sandro Carniel, and N00014-05-1-0759 and N00014-06-1-0287 to Lakshmi Kantha. MS acknowledges the support from the VECTOR-FISR Project; SC gratefully acknowledges the support from the FIRB Project "DECALOGO" (Code RBFR08D828_001) and the partial support from the CNR-RSTL funded project

"MOM". Opportunity to collaborate with NURC and NRL teams is also greatly appreciated. The work of Jeffrey W. Book was supported by the Office of Naval Research as part of the "Dynamics of the Adriatic in Real Time" and "Quantifying Mechanisms of Diapycnal Mixing in Strong Frontal Regions" under Program Elements 0602435 N and 0601153 N, respectively. Many thanks to the Captain and crew of R/V *Alliance* for their unmatched hospitality.

Appendix A. Turbulence measurement details

A.1. Determination of the velocity shear

For velocity shear measurements, the MSS profiler is equipped with two PNS shear sensors. This airfoil type sensor is described in Prandke (2005) and Carniel et al., 2010, and a sketch is presented in Fig. A1. Following Allen and Perkins (1952), for an axially symmetric airfoil in an inviscid flow of speed U and an angle of attack α , the cross force f_p per unit length due to the potential flow can be expressed as

$$f_p = 0.5\rho U^2 \left(\frac{dA}{dx} \right) \sin 2\alpha \quad (A1)$$

where ρ is the density of the fluid and dA/dx is the rate of change in the airfoil cross section area in axial direction. To get the total cross force F , Eq. (A1) can be integrated along the axis from the tip to the position where dA/dx is zero

$$F = 0.5\rho U^2 A \sin 2\alpha \quad (A2)$$

The piezo-ceramic beam voltage output is proportional to the cross-force at the tip of the probe. Thus, the probe sensitivity S can be determined by

$$E_{rms} = SF = \rho S U^2 \sin 2\alpha \quad (A3)$$

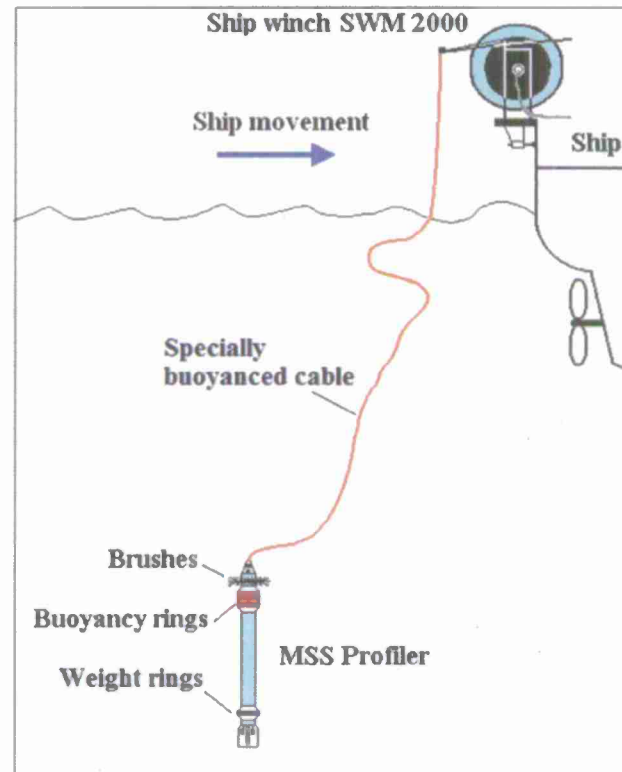


Fig. A1. Sketch of the apparatus employed during the turbulence measurements.

where E_{rms} is the rms voltage output of the shear probe, and the factor 0.5 and A from Eq. (A2) are now included in the sensitivity S . The probe sensitivity S has the dimension $V \text{ m s}^2 \text{ kg}^{-1}$.

The output of the shear probe is an AC voltage signal, however, the calibration is based on rms DC voltage measurement (Eq. (A3)). Consequently, the output of the piezo-ceramic beam E_{beam} can be written as

$$E_{beam} = \sqrt{2} \rho S U^2 \sin 2\alpha = 2\sqrt{2} \rho S V U \quad (\text{A4})$$

where V is the axial component and u is the cross-stream component of the flow speed U , respectively. A simple plot explaining the geometry of the shear probe measurements is shown in Fig. A2. Considering the total gain G of the sensor electronics, the output of the sensor is

$$E_s = 2\sqrt{2} \rho G S V U \quad (\text{A5})$$

The sensor output is a time dependent signal proportional to the temporal change of the velocity cross component. The probe velocity V is assumed to be constant. To obtain the current shear profile, E_s has to be differentiated.

$$\frac{dE_s}{dt} = 2\sqrt{2} \rho G S V \frac{du}{dt} \quad (\text{A6})$$

The shear profile can be obtained using $du/dt = V(du/dz)$ rearrangement of Eq. (A6) gives

$$\frac{du}{dz} = (2\sqrt{2} \rho G S V^2)^{-1} \frac{dE_s}{dt} \quad (\text{A7})$$

The sinking velocity V is calculated from the pressure and time channels. A mean density of 1010 kg/m^3 is been used. The linear trend in the shear profiles is removed (detrending over 1024 data lines = 1 Hz).

A.2. Dissipation rate of TKE and diffusivities

The dissipation rate ε for isotropic turbulence has been calculated from the shear values using the equation for isotropic

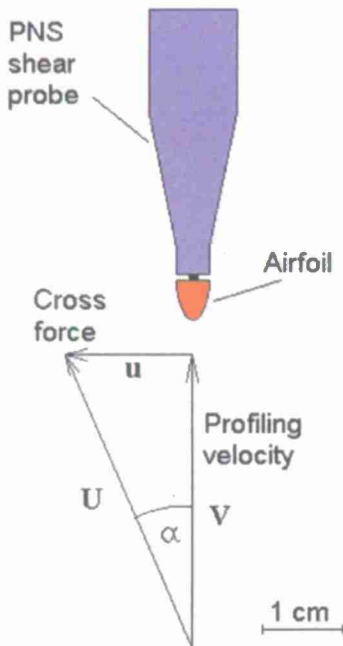


Fig. A2. The geometry of shear probe measurements.

turbulence (see Gregg, 1987; Peters et al., 2007)

$$\varepsilon = 7.5 \nu \left(\frac{du}{dz} \right)^2 \quad (\text{A8})$$

where ν is the kinematic viscosity of water (to be calculated from temperature) and du/dz is the velocity shear. The viscosity was determined from the temperature using a polynomial approximation

$$\nu = 1.792747 - 0.05126103T + 0.0005918645T^2 \quad (\text{A9})$$

where T is the temperature in $^{\circ}\text{C}$ and the viscosity ν is in $10^{-6} \text{ m}^2 \text{ s}^{-1}$.

The velocity shear variance is calculated by integrating the power spectrum in the wave number range from 2 to 30 cpm. The limitation of the high wave number cutoff to 30 cpm is due to narrow band vibration peaks in the wave number range above 30 cpm resulting from eddy generation—at the probe guard of the profiler. The low wave number cutoff at 2 cpm is to eliminate contributions from low frequent tumbling motions of the profiler. The calculated dissipation rates have been corrected for the unresolved low wave number range (cutoff at 2 cpm) and high wave number range (cutoff at 30 cpm) of the spectrum, using correction coefficients obtained from the universal turbulence spectrum (Nasmyth, 1970; Oakey, 1982).

The variance has been calculated in bins of 512 data records (corresponding to approx. 0.3 m depth intervals), with 256 records overlap of the depth bins. Finally, 0.5 dbar depth bins of the dissipation rates have been calculated.

The dissipation rate calculation has been carried out for both shear sensors #1 and #2, and the calculated dissipation rates showed a good agreement. A mean dissipation profile has been calculated from both dissipation profiles. However, in some profiles spikes occurred in one of the two dissipation profiles. We assume a hit of larger particles (which frequently could be seen in the near surface water) to be a reason for the isolates spikes. To eliminate an influence of these spikes in the mean dissipation profile calculated from the two sensors, the following procedure was applied: a mean dissipation value has been calculated if the values of one sensor did not exceed the other one by a factor of 5. If one sensor was larger by a factor of more than 5 in the respective depth interval, the smaller value was taken for the mean profile.

Finally, all mean dissipation profiles have been inspected visually. In depth ranges of particular high dissipation values, the vertical profiles of the shear data and the profiler acceleration were checked. If the high dissipation values were correlated with particular high profiler vibration or extreme amplitudes in the shear signal (e.g., caused by large particles in the water), the calculated dissipation was substituted by interpolated values.

The dissipation rate χ of the microstructure temperature variance has been computed from (Gregg 1987)

$$\chi = 6\kappa_T \left(\frac{dT}{dz} \right)^2 \quad (\text{A10})$$

κ_T is the molecular diffusivity for heat in seawater ($1.4 \times 10^{-7} \text{ m}^2 \text{ s}^{-1}$). For a discussion of the uncertainties and limitations in measuring ε and χ , see Gregg (1999), see also Moum et al., 1995.

For estimating the length scale of turbulent overturns in stratified turbulence, we used the Thorpe scale (see Thorpe, 1977). The density profile for 0.1 m depth intervals has been calculated from the CTD sensors of the MSS. This profile has been reordered to obtain a monotonic profile without density inversions. The Thorpe displacement d is the vertical displacement to achieve a static stable profile. The Thorpe scale L_T has been

computed as the root mean square of the Thorpe displacements for 0.5 dbar intervals.

All hydrographic parameters have been calculated at 0.5 dbar intervals. Salinity and density (σ_t) have been computed from temperature (PT 100), conductivity (7-pole cell) and pressure following EOS80. The Brunt–Väisälä frequency has been calculated following (Gill 1982):

$$N^2 = g\alpha \left(\frac{dT}{dz} + \Gamma \right) - g\beta \frac{ds}{dz} \quad (A11)$$

where g is the gravity constant, α is the thermal expansion coefficient, Γ is the adiabatic lapse rate and β is the expansion coefficient for salinity s . α , Γ and β were computed following EOS80.

Eddy diffusivities have been calculated at 0.5 dbar depth intervals from dissipation rates using

$$K_p = \gamma \varepsilon N^{-2} \quad (A12)$$

following Osborn (1980), see also Gregg (1987), where N is the buoyancy frequency, ε is the dissipation rate and γ is the mixing efficiency, chosen to be a constant equal to 0.2, even though the exact value is somewhat uncertain. An additional independent estimate for the eddy diffusivity, based on the assumption that the Thorpe scale is proportional to the Ozmido scale is given by

$$K_{p,T} = cL_T^2 N \quad (A13)$$

Eqs. (5) and (A12) suggest a value of 0.006 for c .

The dissipation rate χ of the temperature variance $\overline{\theta^2}$ was also measured (Gregg 1987) and the eddy diffusivity of heat K_h was estimated from χ and the vertical temperature gradient, following Osborn and Cox (1972):

$$K_h = \frac{\chi}{2} \left(\frac{dT}{dz} \right)^{-2} \quad (A14)$$

Both K_p and K_h are measures of the intensity of turbulent mixing, and generally track each other well (Peters et al., 1988).

For examples of use of this type of microstructure profiler, see Lass et al. (2003), Burchard et al. (2002), Carniel et al. (2010).

References

Allen, H.J., Perkins, E.W., 1952. A study of effects of flow over slender inclined bodies of revolution. Report No. 1048, U.S. National Advisory Committee for Aeronautics.

Anis, A., Moum, J.N., 1995. Surface wave–turbulence interactions, scaling $\varepsilon(z)$ near the sea surface. *J. Phys. Oceanogr.* 25, 2025–2045.

Book, J.W., Martin, P., Rixen, M., Dykes, J., Wang, D., Ladner, S., Tudor, M., Chiggiato, J., 2008. Real-Time Coastal Monitoring and Prediction for Operations and Research, in 2007 NRL Review, Naval Research Laboratory, 4555 Overlook Ave., SW, Washington, DC 20375–5320, pp. 187–190.

Book, J.W., Signell, R.P., Perkins, H., 2007. Measurements of storm and nonstorm circulation in the northern Adriatic: October 2002 through April 2003. *J. Geophys. Res.* 112, C11592, doi:10.1029/2006JC003556.

Brainerd, K.E., Gregg, M.C., 1993a. Diurnal restratification and turbulence in the oceanic mixed layer, 1. Observations. *J. Geophys. Res.* 98, 22645–22656.

Brainerd, K.E., Gregg, M.C., 1993b. Diurnal restratification and turbulence in the oceanic mixed layer, 2. Modeling. *J. Geophys. Res.* 98, 22657–22666.

Burchard, H., Bolding, K., Rippeth, T.P., Stips, A., Simpson, J.H., Sundermann, J., 2002. Microstructure of turbulence in the northern North Sea: a comparative study of observations and model simulations. *J. Sea Res.* 47, 223–238.

Burrage, D.M., Book, J.W., Martin, P.J., 2009. Eddies and filaments of the Western Adriatic Current near Cape Gargano: Analysis and prediction. *J. Marine Syst.* 78, 5205–5226, doi:10.1016/j.jmarsys.2009.01.024.

Budikov, K., 1974. Climate and Life. Academic Press, 508 pp.

Caldwell, D.R., 1983. Oceanic turbulence: Big bangs or continuous creation? *J. Geophys. Res.* 88, 7453–7550.

Carniel, S., Kantha, L.H., Bergamasco, A., Prandke, H., Small, R.J., Sclavo, M., 2010. Layered structures in the upper Ligurian Sea. *Il Nuovo Cimento* 1258 (10), 1567–1586, doi:10.1393/nc/2010-11113-7.

Carniel, S., Sclavo, M., Kantha, L.H., Clayton, C.A., 2005. Langmuir cells and mixing in the upper ocean. *Il Nuovo Cimento* 28C (1), 33–54, doi:10.1393/ncc/2005-10022-8.

Carniel, S., Sclavo, M., Kantha, L.H., Prandke, H., 2008. Double-Diffusive Layers in the Adriatic Sea. *Geophys. Res. Lett.* 35, L02605, doi:10.1029/2007GL032389.

Dillon, T.M., 1982. Vertical overturns: a comparison of Thorpe and Ozmido length scales. *J. Geophys. Res.* 85, 9601–9613.

Dillon, T.M., Richman, J.G., Hansen, C.G., Pearson, M.D., 1981. Near-surface turbulence measurements in a lake. *Nature* 290, 390–392.

Fairall, C.W., Bradley, E.F., Rogers, D.P., Edson, J.B., Young, G.S., 1996. Bulk parameterization of air-sea fluxes for tropical Ocean–Global atmosphere coupled–ocean atmosphere response experiment. *J. Geophys. Res.* 101 (C2), 3747–3764.

Fer, L., Skogseth, R., Haugan, P.M., 2004. Mixing of the Storjorden overflow (Svalbard Archipelago) inferred from density overturns. *J. Geophys. Res.* 109, 1–14.

Ferron, B., Mercier, H., Speer, K., Gargett, A., Polzin, K., 1998. Mixing in the Romanche fracture zone. *J. Phys. Oceanogr.* 28, 1929–1945.

Galbraith, P.S., Kelly, D.E., 1996. Identifying overturns in CTD profiles. *J. Atmos. Ocean. Technol.* 13, 688–702.

Gargett, A.E., 1999. Velcro measurements of turbulent kinetic energy dissipation rate. *J. Atmos. Ocean. Technol.* 16, 1973–1993.

Gill, A.E., 1982. Atmosphere–Ocean Dynamics. Academic Press.

Gregg, M.C., 1987. Diapycnal mixing in the thermocline: a review. *J. Geophys. Res.* 92, 5249–5286.

Gregg, M.C., 1999. Uncertainties and limitations in measuring ε and χ_T . *J. Atmos. Ocean. Technol.* 16, 1483–1490.

Hebert, D., Moum, J.N., 1994. Decay of a near-inertial wave. *J. Phys. Oceanogr.* 24, 2334–2351.

Hosegood, P.J., Gregg, M.C., Alford, M.H., 2008. Restratiification of the surface mixed layer with submesoscale lateral density gradients: diagnosing the importance of the horizontal dimension. *J. Phys. Oceanogr.* 38, 2438–2460, doi:10.1175/2008JPO3843.1.

Kantha, L.H., 1980. Turbulent entrainment at a buoyancy interface due to convective turbulence. In: Freeland, H.J., Farmer, D.M., Levings, C.D. (Eds.), *Fjord Oceanography*. Plenum Press, pp. 205–214.

Kantha, L.H., 1995. A numerical model of Arctic leads. *J. Geophys. Res.* 100, 4653–4672.

Kantha, L.H., Clayton, C.A., 2004. On the effect of surface gravity waves on mixing in an oceanic mixed layer. *Ocean Modelling* 6, 101–124.

Kantha, L.H., Hocking, W., 2011. Dissipation rates of turbulence kinetic energy in the free atmosphere: MST radar and radiosondes. *J. Atmos. Solar–Terrestrial Phys.* In press, doi:10.1016/j.jastp.2010.11.024.

Kantha, L.H., Lass, H., Prandke, H., 2010. A note on stokes production of turbulence kinetic energy in the oceanic mixed layer: observations in the Baltic Sea. *Ocean Dyn.* 60, 171–180, doi:10.1007/s10236-009-0257-7.

Kunze, E., Schmitt, R.W., Toole, J.M., 1995. The energy balance in a warm-core ring's near-inertial critical layer. *J. Phys. Oceanogr.* 25, 942–957.

Lass, H.U., Prandke, H., Liljebladh, B., 2003. Dissipation in the Baltic proper during winter stratification. *J. Geophys. Res.* 108 (C6), 3187, doi:10.1029/2002JC001401.

Lee, C.M., Askari, F., Book, J., Carniel, S., Cushman-Roisin, B., Dorman, C., et al., 2005. Northern Adriatic response to a wintertime bora wind event. *EOS, Trans. Am. Geophys. Union*, 86, 157, 163, 165.

Longmardo, C.P., Gregg, M.C., 1989. Similarity scaling of viscous and thermal dissipation in a convecting surface boundary layer. *J. Geophys. Res.* 94, 6273–6284.

Lozovatsky, I., Figueira, M., Roget, E., Fernando, H.J.S., Shapovalov, S., 2005. Observations and scaling of the upper mixed layer in the North Atlantic. *J. Geophys. Res.* 110, C05013.

Magaldi, M.G., Özgökmen, T.M., Griffa, A., Rixen, M., 2010. On the response of a turbulent coastal buoyant current to wind events: the case of the Western Adriatic Current. *Ocean Dyn.* 60, 93–122, doi:10.1007/s10236-009-0247-9.

Moum, J.N., 1996. Energy-containing scales of turbulence in the ocean thermocline. *J. Geophys. Res.* 101, 14095–14101.

Moum, J.N., Gregg, M.C., Lien, R.C., Carr, M.E., 1995. Comparison of turbulence kinetic energy dissipation rate estimates from two ocean microstructure profilers. *J. Atmos. Oceanic Technol.* 12, 346–366.

Nasmyth, P.W., 1970. Oceanic Turbulence. Ph.D. thesis, University of British Columbia, Vancouver, 8.C.

Oakey, N.S., 1982. Determination of the rate of dissipation of turbulent energy from simultaneous temperature and velocity shear microstructure measurements. *J. Phys. Oceanogr.* 12, 256–271.

Osborn, T.R., 1980. Estimates of the local rate of vertical diffusion from dissipation measurements. *J. Phys. Oceanogr.* 10, 83–89.

Osborn, T.R., Cox, C.S., 1972. Oceanic fine structure. *Geophys. Fluid Dyn.* 3, 321–345.

Payne, R.E., 1972. Albedo of the sea surface. *J. Atmos. Sci.* 29, 959–970.

Peters, H., Orlitz, M., 2005. Ocean mixing in the springtime central Adriatic Sea. *Geofizika* 22, 1–19.

Peters, H., Gregg, M.C., Toole, J.M., 1988. On the parameterization of equatorial turbulence. *J. Geophys. Res.* 93, 1199–1218.

Peters, H., Lee, C.M., Orlitz, M., Dorman, C.E., 2007. Turbulence in the wintertime northern Adriatic Sea under strong atmospheric forcing. *J. Geophys. Res.* 112 (C6), C06599.

Pollard, R.T., Rhines, P.B., Thompson, O.R.Y., 1973. The deepening of the wind-mixed layer. *Geophys. Fluid Dyn.* 3, 381–404.

Prandke, H., 2005. Microstructure sensors. In: Baumert, H., Simpson, J., Sundermann, J. (Eds.), *Marine Turbulence: Theories, Models, and Observations*. Cambridge University Press, pp. 101–109.

Prandke, H., Holtsch, K., Stips, A., 2000. MITEC Report Technical Note No. I.96.87, European Commission, Joint Research Centre, Space Applications Institute, Ispra/Italy.

Signell, R.P., Carniel, S., Cavalieri, L., Chiggiato, J., Doyle, J.D., Pullen, J., Sclavo, M., 2005. Assessment of wind quality for oceanographic modelling in semi-enclosed basins. *J. Mar. Syst.* 53 (1–4), 217–233.

Shay, T.J., Gregg, M.C., 1984. Turbulence in an oceanic convective mixed layer. *Nature* 310, 282–285.

Shay, T.J., Gregg, M.C., 1986. Convectively driven turbulent mixing in the upper ocean. *J. Phys. Oceanogr.* 16, 1777–1798.

Stips, A., Burchard, H., Bolding, K., Eifler, W., 2002. Modelling of convective turbulence with two-equation $k-\epsilon$ turbulence closure scheme. *Ocean Dyn.* 52, 153–168.

Taillardier, V., Griffa, A., Poulaïn, P.-M., Signell, R., Chiggiato, J., Carniel, S., 2008. Variational analysis of drifter positions and model outputs for the reconstructions of surface currents in the central Adriatic during fall 2002. *J. Geophys. Res.* 113, C04004, doi:10.1029/2007JC04148.

Thorpe, S.A., 1977. Turbulence and mixing in a Scottish Loch. *Philos. Trans. R. Soc. London, Ser. A* 286, 125–181.

Thorpe, S.A., 2005. The Turbulent Ocean. Cambridge University Press 439pp.

Tillmar, N., Alfredsson, P.H., 1993. Turbulence in plane Couette flow. *Appl. Sci. Res.* 51, 237–241.

Wesson, J.C., Gregg, M.C., 1994. Mixing in the Camarinal Sill in the Strait of Gibraltar. *J. Geophys. Res.* 99, 9847–9878.

REPORT DOCUMENTATION PAGE

Form Approved
OMB No. 0704-0188

The public reporting burden for this collection of information is estimated to average 1 hour per response, including the time for reviewing instructions, searching existing data sources, gathering and maintaining the data needed, and completing and reviewing the collection of information. Send comments regarding this burden estimate or any other aspect of this collection of information, including suggestions for reducing the burden, to the Department of Defense, Executive Services and Communications Directorate (0704-0188). Respondents should be aware that notwithstanding any other provision of law, no person shall be subject to any penalty for failing to comply with a collection of information if it does not display a currently valid OMB control number.

PLEASE DO NOT RETURN YOUR FORM TO THE ABOVE ORGANIZATION.

1. REPORT DATE (DD-MM-YYYY) 05-12-2012	2. REPORT TYPE Journal Article	3. DATES COVERED (From - To)				
4. TITLE AND SUBTITLE Turbulence Variability in the Upper Layers of the Southern Adriatic Sea Under A Variety of Atmospheric Forcing Conditions		5a. CONTRACT NUMBER	5b. GRANT NUMBER			
		5c. PROGRAM ELEMENT NUMBER 0602435N	5d. PROJECT NUMBER			
		5e. TASK NUMBER	5f. WORK UNIT NUMBER 73-6648-07-5			
7. PERFORMING ORGANIZATION NAME(S) AND ADDRESS(ES) Naval Research Laboratory Oceanography Division Stennis Space Center, MS 39529-5004			8. PERFORMING ORGANIZATION REPORT NUMBER NRL/JA/7330-08-8346			
9. SPONSORING/MONITORING AGENCY NAME(S) AND ADDRESS(ES) Office of Naval Research 800 N. Quincy St. Arlington, VA 22217-5660			10. SPONSOR/MONITOR'S ACRONYM(S) ONR			
			11. SPONSOR/MONITOR'S REPORT NUMBER(S)			
12. DISTRIBUTION/AVAILABILITY STATEMENT Approved for public release, distribution is unlimited.						
13. SUPPLEMENTARY NOTES						
14. ABSTRACT As part of the DART06B observational campaign in late August 2006, a microstructure profiler was deployed to make turbulence measurements in the upper layers of the Southern Adriatic Sea. Of the nearly 300 total casts, 163 were made near Station B90, where various moorings were deployed in the 90 m deep water column to measure water column properties and meteorological and surface wave conditions. We were able to measure turbulence properties in the upper layers under a variety of atmospheric forcing conditions that included strong wind forcing, night-time convection, mixed convection and wind forcing, weak wind forcing and strong insolation. The resulting dataset provides a kaleidoscope of turbulence properties and turbulent mixing above, below and in the strong pycnocline present at a depth of 15 -25 m in the coastal waters of the Southern Adriatic Sea during late summer. A slightly modified scaling of the dissipation rate of turbulence kinetic energy in the Mixed Layer (ML), based on the observed friction velocity u_* and the surface buoyancy flux J_{b0} , reproduces the measured values reasonably well. In the interior, below the ML, the dissipation rate scales like $L_T^2 N^3$, where L_T is the Thorpe scale and N is the buoyancy frequency. Analysis of velocity and density profile measurements from Station B90 and the nearby Station B75 suggest that anticyclonic eddies and near-inertial waves can interact in these coastal waters to produce significant horizontal advective density fluxes in the pycnocline.						
15. SUBJECT TERMS turbulent mixing, micro structure, mixing processes						
16. SECURITY CLASSIFICATION OF: a. REPORT Unclassified		b. ABSTRACT Unclassified	c. THIS PAGE Unclassified	17. LIMITATION OF ABSTRACT UL	18. NUMBER OF PAGES 18	19a. NAME OF RESPONSIBLE PERSON Jeffrey Book
					19b. TELEPHONE NUMBER (Include area code) 228-688-5251	